# High order finite difference scheme with explicit-implicit-null time-marching for the compressible Navier-Stokes equations

Meiqi Tan[1], Juan Cheng[2], and Chi-Wang Shu[3]

**Abstract**

The compressible Navier-Stokes (CNS) equations play an important role in the widespread applications of fluid mechanics. In this paper, a high order finite difference scheme with explicit-implicit-null (EIN) time-marching is proposed for the CNS equations in generalized coordinates. High order in space is achieved by using a fifth order weighted essentially non-oscillatory scheme for the inviscid terms, and fourth order central difference schemes for the viscous terms. The main idea of the EIN method discussed in this paper is to add and subtract an appropriately large Laplacian operator at one side of the considered system, and then apply an implicit-explicit time-marching method to the equivalent equations. Coupled with the finite difference discretizations, the resulting scheme is very suitable for problems, where nonlinear viscosity dominates or partially dominates, as the viscous terms are treated explicitly. Moreover, being implicit-explicit in time, it can achieve a more relaxed time step restriction than fully explicit methods. A number of numerical experiments are given to demonstrate the desired properties of the proposed scheme such as loose stability constraints, high order accuracy and non-oscillation.

**Keywords:** Navier-Stokes equations, explicit-implicit-null time discretization, finite difference method, stability, high order.

[1]Graduate School, China Academy of Engineering Physics, Beijing 100088, China. E-mail: tanmeiqi20@gscaep.ac.cn.

[2]Corresponding author. Laboratory of Computational Physics, Institute of Applied Physics and Computational Mathematics, Beijing 100088, China and HEDPS, Center for Applied Physics and Technology, and College of Engineering, Peking University, Beijing 100871, China. E-mail: cheng_juan@iapcm.ac.cn. Research is supported in part by National Key R&D Program of China No. 2023YFA1009003, and NSFC grant 12031001.

[3]Division of Applied Mathematics, Brown University, Providence, RI 02912, USA. E-mail: chi-wang_shu@brown.edu. Research is supported in part by NSF grant DMS-2309249.

# 1 Introduction

The compressible Navier-Stokes (CNS) equations play an important role in the widespread applications of fluid mechanics. The applications ranging from aerospace to mechanical engineering as well as environmental engineering constitute an active research field that requires the numerical solutions of the equations.

One of the difficulties in computing the CNS equations is the stiffness caused by the viscous terms. If explicit methods are used, the computations will become inefficient because the schemes will suffer from a parabolic time step restriction which might become very severe for high viscosity coefficients and small mesh sizes. In such cases, one may resort to implicit time discretization. Stable implicit methods exist for virtually any order and they are usually free of time step restriction. However, the implementation of implicit methods implies the solutions of large nonlinear systems which could be computationally very expensive. Furthermore, the employment of high order schemes in space complicates the realization of such methods. All the above comments on the explicit and implicit methods suggest that both methods may be coupled to take benefit from each other in its best domain of confidence. The explicit-implicit (IMEX) method is a typical example that adopts this idea. In the case of viscous-dominated problems, the IMEX methods [16, 22, 23, 27] treat the viscous terms implicitly and the inviscid terms explicitly, thereby avoiding severe parabolic restrictions on the maximum admissible time step. However, for the equations with nonlinear viscosity coefficients, the method still involves the solution of large nonlinear algebraic systems and hence is still expensive to use. As a consequence, a lot of effort has been devoted to the construction of the semi-implicit and explicit-implicit-null (EIN) methods, which represent strategies that can linearly handle equations with nonlinear stiff terms. The readers can refer to [3–6] and the references therein for details of the semi-implicit method. In this paper we will focus on the EIN method for the CNS equations.

Considering a problem of the form

$$\frac{\mathrm{d}\boldsymbol{U}}{\mathrm{d}t} = f(t, \boldsymbol{U}),$$

where the right-hand side $f(t, \boldsymbol{U})$ represents the remaining terms in the equations apart from the time derivatives, the EIN method is obtained by first identifying a mode which may produce stiffness. Then a simple approximation to the terms producing this mode is added and subtracted from one side of the equation

$$\frac{\mathrm{d}\boldsymbol{U}}{\mathrm{d}t} = \underbrace{f(t, \boldsymbol{U}) - g(t, \boldsymbol{U})}_{\mathcal{T}_1} + \underbrace{g(t, \boldsymbol{U})}_{\mathcal{T}_2}.$$

Finally, the EIN method is completed by applying the standard IMEX method to the above equation. The term $g(t, \boldsymbol{U})$ is well-chosen to remove the stiffness in $f(t, \boldsymbol{U})$ such that $\mathcal{T}_1$ is either not stiff, or less stiff compared to $\mathcal{T}_2$, thus allows for an explicit treatment, and $\mathcal{T}_2$ is stiff and preferably linear, thus will be discretized implicitly. Since the term $g(t, \boldsymbol{U})$ that is added to the equation is then subtracted (seemingly adding zero), Duchemin and Eggers [12] proposed to call this approach the "explicit-implicit-null method", or EIN method for short. The selection of the term $g(t, \boldsymbol{U})$ is quite flexible, but needs to have the same scaling in wave number as the stiff terms to be resolved.

The EIN method has been implemented previously by a number of authors on a case-by-case basis for the scalar equations [11, 26, 30, 32–34]. The method has also been used for the compressible magnetohydrodynamic equations in three dimensions [18], but only has first order accuracy. The discussions of the EIN method on the Euler and Navier-Stokes equations can be found in [8, 10, 14, 17, 24]. In these papers, the EIN method is obtained by adding and subtracting a gradient-type term at one side of the system, since the authors are more concerned about the stiffness induced by the low Mach numbers. As we are more interested in time scales where viscous effects play an important relevant role, we add and subtract an appropriately large Laplacian operator at one side of the CNS equations, and then treat them separately using the standard formalism of the IMEX method. The EIN method designed in this way is very suitable for problems where nonlinear viscosity dominates or partially

dominates, as it gives rise to a linear system for which very efficient solution methods exist. Being implicit-explicit in time, it can achieve a more relaxed time step restriction than fully explicit methods. In addition, it is worth mentioning that the method is not limited by the equation of state (EOS). To the best of our knowledge, the EIN method so designed for the CNS equations has not been studied before.

With regard to the spatial discretizations, we choose the finite difference schemes because of its simplicity in design and coding. Specifically, the fourth order central difference schemes are employed for the viscous terms. For the inviscid terms, a fifth order weighted essentially non-oscillatory (WENO) scheme [19, 28] is adopted. The WENO scheme is constructed based on the Lax-Friedrichs flux splitting method. To avoid spurious numerical oscillations in the presence of shock waves and other discontinuities, the method of local characteristic decomposition is used. We make sure that the approximations of all the spatial derivatives are in a flux-difference form, so that the local and global conservation of mass, momentum and energy are guaranteed.

The outline of the paper unfolds as follows. After the introductory section, the governing equations and the assumptions made are presented. In Section 3, we first describe the details of the time and space discretizations, and then we discuss the linear stability properties of the full scheme. Numerical tests are shown in Section 4. Finally, a concluding section finalizes the paper.

# 2 Governing equations

For a Cartesian coordinate system, where $u$, $v$ represent the $x$, $y$ components of the velocity vector, the two-dimensional compressible Navier-Stokes equations can be written in a conservation-law form

$$\frac{\partial \boldsymbol{U}}{\partial t} + \frac{\partial \boldsymbol{F}_1}{\partial x} + \frac{\partial \boldsymbol{F}_2}{\partial y} = \frac{\partial \boldsymbol{F}_{\mu,1}}{\partial x} + \frac{\partial \boldsymbol{F}_{\mu,2}}{\partial y} \tag{2.1}$$

where the conserved variable vector $\boldsymbol{U}$, the inviscid flux vectors $\boldsymbol{F}_1$ and $\boldsymbol{F}_2$, and the viscous flux vectors $\boldsymbol{F}_{\mu,1}$ and $\boldsymbol{F}_{\mu,2}$ are defined as

$$\boldsymbol{U} = \begin{pmatrix} \rho \\ \rho u \\ \rho v \\ E \end{pmatrix}, \quad \boldsymbol{F}_1 = \begin{pmatrix} \rho u \\ \rho u^2 + p \\ \rho uv \\ u(E+p) \end{pmatrix}, \quad \boldsymbol{F}_2 = \begin{pmatrix} \rho v \\ \rho uv \\ \rho v^2 + p \\ v(E+p) \end{pmatrix}, \tag{2.2a}$$

$$\boldsymbol{F}_{\mu,1} = \begin{pmatrix} 0 \\ \tau_{xx} \\ \tau_{yx} \\ u\tau_{xx} + v\tau_{xy} + \kappa T_x \end{pmatrix}, \quad \boldsymbol{F}_{\mu,2} = \begin{pmatrix} 0 \\ \tau_{xy} \\ \tau_{yy} \\ u\tau_{yx} + v\tau_{yy} + \kappa T_y \end{pmatrix}. \tag{2.2b}$$

Here, the quantities $(\cdot)_x = \partial(\cdot)/\partial x$ and $(\cdot)_y = \partial(\cdot)/\partial y$ are the corresponding partial derivatives of the variable $(\cdot)$, $T$ denotes the temperature, $\rho$ is the mass density, $p$ denotes the fluid pressure, $E$ is the total energy per unit volume which can also be rewritten as

$$E = \rho\frac{u^2 + v^2}{2} + \rho e,$$

with $e$ the specific internal energy. We assume that the fluid is Newtonian, then components of the viscous stress tensor are given under the Stokes' hypothesis by

$$\begin{aligned} \tau_{xx} &= \frac{2}{3}\mu\left(2\frac{\partial u}{\partial x} - \frac{\partial v}{\partial y}\right), \\ \tau_{yy} &= \frac{2}{3}\mu\left(2\frac{\partial v}{\partial y} - \frac{\partial u}{\partial x}\right), \\ \tau_{xy} &= \mu\left(\frac{\partial u}{\partial y} + \frac{\partial v}{\partial x}\right) = \tau_{yx}, \end{aligned}$$

where $\mu$ denotes the coefficient of viscosity which depends strongly on the temperature $T$. In this paper, the relation between $\mu$ and $T$ is governed by the Sutherland's law, that is

$$\mu(T) = \mu_T \left(\frac{T}{T_\mu}\right)^\beta \frac{T_\mu + S_\mu}{T + S_\mu}, \tag{2.3}$$

with parameters $\mu_T$, $T_\mu$, $\beta$ and $S_\mu$. Note that constant viscosity $\mu_T$ is retrieved if $\beta = 1$ and $S_\mu = 0$. Under the assumption that the specific heat at constant pressure $c_p$ is constant, the coefficient of thermal conductivity $\kappa$ is linked to the viscosity coefficient $\mu$ by a constant Prandtl number $Pr$, that is

$$\kappa = \frac{\mu c_p}{Pr}.$$

In order to construct the numerical scheme in curvilinear coordinates, the coordinate transformation from the physical domain $(x, y)$ to the computational domain $(\xi, \eta)$ is considered. Assume that $J$ denotes the determinant of the transformation matrix

$$J = \det\left(\frac{\partial(x,y)}{\partial(\xi,\eta)}\right) = x_\xi y_\eta - x_\eta y_\xi,$$

the equations (2.1) can be transformed as

$$\frac{\partial J\boldsymbol{U}}{\partial t} + \frac{\partial \boldsymbol{G}_1}{\partial \xi} + \frac{\partial \boldsymbol{G}_2}{\partial \eta} = \frac{\partial \boldsymbol{G}_{\mu,1}}{\partial \xi} + \frac{\partial \boldsymbol{G}_{\mu,2}}{\partial \eta}, \tag{2.4}$$

where the inviscid flux vectors $\boldsymbol{G}_1$ and $\boldsymbol{G}_2$, and the viscous flux vectors $\boldsymbol{G}_{\mu,1}$ and $\boldsymbol{G}_{\mu,2}$ are defined by

$$\begin{aligned} \boldsymbol{G}_1 &= y_\eta \boldsymbol{F}_1 - x_\eta \boldsymbol{F}_2, \qquad & \boldsymbol{G}_2 &= x_\xi \boldsymbol{F}_2 - y_\xi \boldsymbol{F}_1, \\ \boldsymbol{G}_{\mu,1} &= y_\eta \boldsymbol{F}_{\mu,1} - x_\eta \boldsymbol{F}_{\mu,2}, \qquad & \boldsymbol{G}_{\mu,2} &= x_\xi \boldsymbol{F}_{\mu,2} - y_\xi \boldsymbol{F}_{\mu,1}. \end{aligned}$$

Here, the quantities $(\cdot)_\xi = \partial(\cdot)/\partial\xi$ and $(\cdot)_\eta = \partial(\cdot)/\partial\eta$ are the corresponding partial derivatives of the variable $(\cdot)$. For the governing equations (2.4), we have the following elementary result.

**Proposition 2.1.** *Assume that*

$$\boldsymbol{D} = \begin{pmatrix} \frac{\partial \boldsymbol{G}_{\mu,1}}{\partial \boldsymbol{U}_\xi} & \frac{\partial \boldsymbol{G}_{\mu,1}}{\partial \boldsymbol{U}_\eta} \\ \frac{\partial \boldsymbol{G}_{\mu,2}}{\partial \boldsymbol{U}_\xi} & \frac{\partial \boldsymbol{G}_{\mu,2}}{\partial \boldsymbol{U}_\eta} \end{pmatrix},$$

*the spectral radius of* $\boldsymbol{D}$ *is*

$$\lambda_\mu^{\max} = \frac{1}{J}\max\left\{\frac{4}{3}(x_\xi^2 + y_\xi^2)\frac{\mu}{\rho},\ \frac{4}{3}(x_\eta^2 + y_\eta^2)\frac{\mu}{\rho},\ \kappa(x_\xi^2 + y_\xi^2)\left|\frac{\partial T}{\partial E}\right|,\ \kappa(x_\eta^2 + y_\eta^2)\left|\frac{\partial T}{\partial E}\right|\right\}. \tag{2.5}$$

For convenience, we restrict the description to the governing equations in two dimension. It is easy to reduce the equations to one dimension.

## 2.1 The equation of state

A thermal equation of state $p = p(T, \rho)$ and a caloric equation of state $e = e(T, \rho)$ are required to close the above system. If we consider the ideal gas, the thermal and caloric

equations of state read, respectively,

$$p = RT\rho, \qquad e = c_v T, \tag{2.6}$$

where $R = c_p - c_v$ denotes the specific gas constant. The coefficient $c_v$ indicates the heat capacity at constant volume, while the quantity $\gamma = c_p/c_v$ is referred to as the ratio of specific heats. The temperature can be eliminated from both expressions in (2.6), thus leading to an EOS of the form

$$p(\rho, e) = (\gamma - 1)\rho e.$$

For some applications the ideal gas law is an accurate approximation. In other cases, a non-ideal gas EOS is required to account for non-ideal gas effects. An example of non-ideal gas EOS is given by the simplified van der Waals EOS in the form of

$$p = \frac{RT\rho}{1 - b_v\rho}, \qquad e = c_v T. \tag{2.7}$$

The constant $b_v$ is the van der Waals excluded volume, and it places a limit, $\max \rho = \frac{1}{b_v}$, on the density of the gas. Similarly, the temperature can be eliminated from both expressions in (2.7), thus leading to an EOS of the form

$$p(\rho, e) = \frac{(\gamma - 1)\rho e}{1 - b_v\rho}.$$

For simplicity, we take $\gamma = 1.4$ for both the ideal gas EOS and the simplified van der Waals EOS. More non-ideal gas equations of state are available in the literature [31].

**Proposition 2.2.** *When the equation of state is in the form of $p = p(\rho, e)$, the spectral radius of $\frac{\partial \boldsymbol{G}_1}{\partial \boldsymbol{U}}$ is*

$$\lambda_{c,1}^{\max} = \max\left\{\left|y_\eta u - x_\eta v \pm c_s\sqrt{x_\eta^2 + y_\eta^2}\right|\right\}, \tag{2.8a}$$

*and the spectral radius of $\frac{\partial \boldsymbol{G}_2}{\partial \boldsymbol{U}}$ is*

$$\lambda_{c,2}^{\max} = \max\left\{\left|x_\xi v - y_\xi u \pm c_s\sqrt{x_\xi^2 + y_\xi^2}\right|\right\}, \tag{2.8b}$$

*with the sound speed $c_s = \sqrt{p_\rho + pp_e/\rho^2}$. Here, the quantities $p_\rho$ and $p_e$ denote the partial derivatives $\partial p(\rho, e)/\partial\rho|_e$ and $\partial p(\rho, e)/\partial e|_\rho$, respectively.*

# 3 Numerical scheme

In the preceding section the governing equations and the assumptions made are presented. In this section, we start from the equations (2.4) and provide a specific description of the full space and time discretizations. Subsequently, a linearized stability analysis is performed.

## 3.1 Preliminaries

Assume that the computational domain is covered by a uniform mesh with $N_1$ nodes in the $\xi$-coordinate direction, and $N_2$ nodes in the $\eta$-coordinate direction. The mesh sizes along each direction are denoted by $\Delta\xi$ and $\Delta\eta$, respectively. The physical domain is covered by a mesh, which is the image of the computational mesh via the coordinate transformation mapping. Generally, the physical mesh is not uniform, but is smooth and retains the same mesh connectivity structure as the computational mesh.

## 3.2 Discretization of the inviscid terms

To achieve high order accuracy in space, a fifth order finite difference flux splitting WENO scheme [19, 28] is employed for the inviscid terms, $\frac{\partial \boldsymbol{G}_1}{\partial \xi}$ and $\frac{\partial \boldsymbol{G}_2}{\partial \eta}$. For numerical simulations of flow fields containing shocks and other discontinuities, the component by component version of the WENO scheme may still lead to oscillatory results and a Roe-type local characteristic decomposition [15], even though more costly, may effectively eliminate such spurious oscillations. For brevity, only the procedures for computing $\frac{\partial \boldsymbol{G}_1}{\partial \xi}$ are described. The derivative $\frac{\partial \boldsymbol{G}_2}{\partial \eta}$ is treated analogously.

We let $\boldsymbol{G}_{1,j,k}$ be the point value of the flux function $\boldsymbol{G}_1$ at the grid point $(\xi_j, \eta_k)$. To approximate $\left.\frac{\partial \boldsymbol{G}_1}{\partial \xi}\right|_{\xi_j,\eta_k}$, we fix the $k$-index and approximate it in a flux-difference form, i.e.,

$$\left.\frac{\partial \boldsymbol{G}_1}{\partial \xi}\right|_{\xi_j,\eta_k} = \frac{1}{\Delta\xi}\left(\hat{\boldsymbol{G}}_{1,j+\frac{1}{2},k} - \hat{\boldsymbol{G}}_{1,j-\frac{1}{2},k}\right) + O(\Delta\xi^5),$$

where $\hat{\boldsymbol{G}}_{1,j\pm\frac{1}{2},k} = \hat{\boldsymbol{G}}^{+}_{1,j\pm\frac{1}{2},k} + \hat{\boldsymbol{G}}^{-}_{1,j\pm\frac{1}{2},k}$ are the numerical fluxes defined at the points $(\xi_{j\pm\frac{1}{2}}, \eta_k)$. Here, $\xi_{j\pm\frac{1}{2}} = \xi_j \pm \frac{1}{2}\Delta\xi$. The procedures of obtaining the numerical fluxes $\hat{\boldsymbol{G}}^{\pm}_{1,j+\frac{1}{2},k}$ in the

local characteristic fields can be summarized as follows. At each point $(\xi_{j+\frac{1}{2}}, \eta_k)$, where the computation of the numerical fluxes is needed, we perform the following steps:

1. Construct a Jacobian matrix $\boldsymbol{A}_{j+\frac{1}{2},k}$ and obtain the corresponding eigenvalues $\boldsymbol{\Lambda}_{j+\frac{1}{2},k}$ and right eigenvectors $\boldsymbol{R}_{j+\frac{1}{2},k}$ by following the same course of reasoning as that used in [15]. The left eigenvectors can be obtained as $\boldsymbol{L}_{j+\frac{1}{2},k} = \boldsymbol{R}^{-1}_{j+\frac{1}{2},k}$. However, numerical inversion may be a delicate step. Therefore, the specific expressions for the corresponding left eigenvectors are provided. The results are summarized in the Appendix.

2. Project all the point values which are in the potential stencil of the WENO reconstruction for obtaining $\hat{\boldsymbol{G}}^{\pm}_{1,j+\frac{1}{2},k}$ to the local characteristic fields. For example,

$$\boldsymbol{W}_{l,k} = \boldsymbol{L}_{j+\frac{1}{2},k}\boldsymbol{U}_{l,k}, \quad \boldsymbol{H}_{1,l,k} = \boldsymbol{L}_{j+\frac{1}{2},k}\boldsymbol{G}_{1,l,k}, \quad l \text{ in a neighborhood of } j.$$

3. Perform the scalar flux splitting WENO reconstruction procedure for each component of the characteristic variables to obtain the corresponding component of the fluxes $\hat{\boldsymbol{H}}^{\pm}_{1,j+\frac{1}{2},k}$. Here we use the Lax-Friedrichs flux splitting [28]

$$\boldsymbol{H}^{\pm}_{1,j,k} = \frac{1}{2}(\boldsymbol{H}_{1,j,k} \pm \boldsymbol{\alpha}\boldsymbol{W}_{j,k}),$$

   where $\boldsymbol{\alpha}$ is a diagonal matrix composed of the maximum absolute value of each eigenvalue of $\boldsymbol{\Lambda}_{j+\frac{1}{2},k}$ with respect to $j$.

4. Transform back into the physical space

$$\hat{\boldsymbol{G}}^{\pm}_{1,j+\frac{1}{2},k} = \boldsymbol{R}_{j+\frac{1}{2},k}\hat{\boldsymbol{H}}^{\pm}_{1,j+\frac{1}{2},k}.$$

The procedures are analogous for $\hat{\boldsymbol{G}}^{\pm}_{1,j-\frac{1}{2},k}$.

## 3.3 Discretization of the viscous terms

The second derivatives, for example $\frac{\partial^2 u}{\partial \xi^2}$, can be approximated by a standard fourth order central difference scheme, that is,

$$\left.\frac{\partial^2 u}{\partial \xi^2}\right|_{\xi_j,\eta_k} = \frac{-(u_{j+2,k} + u_{j-2,k}) + 16(u_{j+1,k} + u_{j-1,k}) - 30u_{j,k}}{12\Delta\xi^2} + O(\Delta\xi^4), \tag{3.1}$$

while the mixed derivatives, for example $\frac{\partial^2 u}{\partial \xi \partial \eta}$, can be approximated by the following fourth order central difference scheme in a dimension-by-dimension fashion

$$\left.\frac{\partial u}{\partial \xi}\right|_{\xi_j,\eta_k} = \frac{u_{j-2,k} - 8u_{j-1,k} + 8u_{j+1,k} - u_{j+2,k}}{12\Delta\xi} + O(\Delta\xi^4).$$

To discretize the complex second derivatives, for example $\frac{\partial}{\partial \xi}(\mu \frac{\partial u}{\partial \xi})$, the following fourth order central difference scheme is used

$$\left.\frac{\partial}{\partial \xi}\left(\mu\frac{\partial u}{\partial \xi}\right)\right|_{\xi_j,\eta_k} = \frac{1}{288\Delta\xi^2}\begin{pmatrix}\mu_{j-2,k}\\ \mu_{j-1,k}\\ \mu_{j,k}\\ \mu_{j+1,k}\\ \mu_{j+2,k}\end{pmatrix}^{\top}\begin{pmatrix}1 & -27 & 27 & -1 & 0\\ -25 & 218 & -168 & -26 & 1\\ -1 & 220 & -438 & 220 & -1\\ 1 & -26 & -168 & 218 & -25\\ 0 & -1 & 27 & -27 & 1\end{pmatrix}\begin{pmatrix}u_{j-2,k}\\ u_{j-1,k}\\ u_{j,k}\\ u_{j+1,k}\\ u_{j+2,k}\end{pmatrix} + O(\Delta\xi^4).$$

The scheme is conservative and the standard fourth order central difference scheme (3.1) can be retrieved when $\mu = 1$.

## 3.4 Temporal discretization

The general practice of the EIN method is to add and subtract an appropriately large linear stiff term at one side of the equation, and then apply the IMEX time-marching method to the equivalent equation. Since we are mainly interested in time scales where viscous effects play an important relevant role, we add a Laplacian operator with constant coefficient to both sides of the system (2.4)

$$\frac{\partial J\boldsymbol{U}}{\partial t} + \underbrace{\frac{\partial \boldsymbol{G}_1}{\partial \xi} + \frac{\partial \boldsymbol{G}_2}{\partial \eta} - \frac{\partial \boldsymbol{G}_{\nu,1}}{\partial \xi} - \frac{\partial \boldsymbol{G}_{\nu,2}}{\partial \eta} + a_1\left(\frac{\partial^2 \boldsymbol{U}}{\partial \xi^2} + \frac{\partial^2 \boldsymbol{U}}{\partial \eta^2}\right)}_{\mathcal{T}_1} = \underbrace{a_1\left(\frac{\partial^2 \boldsymbol{U}}{\partial \xi^2} + \frac{\partial^2 \boldsymbol{U}}{\partial \eta^2}\right)}_{\mathcal{T}_2}. \quad (3.2)$$

Here, $a_1$ is an appropriately large constant such that $\mathcal{T}_1$ is either not stiff, or less stiff and less dissipative compared to $\mathcal{T}_2$, thus it can be treated explicitly, and $\mathcal{T}_2$ is stiff and dissipative, thus will be discretized implicitly.

We assume that the semi-discrete scheme of (3.2) are written in the form of a first order ODE system, that is

$$\frac{\mathrm{d}J\boldsymbol{U}}{\mathrm{d}t} = \mathcal{L}(t, \boldsymbol{U}) + \mathcal{N}(t, \boldsymbol{U}), \quad (3.3)$$

where $\mathcal{L}(t, \boldsymbol{U})$ arises from the spatial discretization of $\mathcal{T}_2$, and $\mathcal{N}(t, \boldsymbol{U})$ is derived from the spatial discretization of $\mathcal{T}_1$. We use a third order IMEX Runge-Kutta method introduced in [1] to solve (3.3). Assume that $\boldsymbol{U}^n$ denotes the numerical solution at time $t^n$, the IMEX Runge-Kutta method forms 5 intermediate values $\boldsymbol{U}^{n,m}$, $1 \le m \le 5$ according to

$$J\boldsymbol{U}^{n,m} = J\boldsymbol{U}^n + \Delta t \sum_{l=1}^{m} \tilde{a}_{ml} \mathcal{L}(t_l^n, \boldsymbol{U}^{n,l}) + \Delta t \sum_{l=1}^{m-1} \hat{a}_{ml} \mathcal{N}(t_l^n, \boldsymbol{U}^{n,l}), \tag{3.4a}$$

from which the approximation at $t^{n+1}$ is assembled by

$$J\boldsymbol{U}^{n+1} = J\boldsymbol{U}^n + \Delta t \sum_{l=1}^{5} \tilde{b}_l \mathcal{L}(t_l^n, \boldsymbol{U}^{n,l}) + \Delta t \sum_{l=1}^{5} \hat{b}_l \mathcal{N}(t_l^n, \boldsymbol{U}^{n,l}). \tag{3.4b}$$

The intermediate values $\boldsymbol{U}^{n,m}$, $1 \le m \le 5$ are approximations to $\boldsymbol{U}(t_m^n)$ and

$$t_m^n = t^n + c_m \Delta t, \qquad c_m = \sum_{l=1}^{m} \tilde{a}_{ml} = \sum_{l=1}^{m-1} \hat{a}_{ml}.$$

The IMEX Runge-Kutta method used in this paper is characterized by matrices $(\tilde{a}_{ml})_{5\times5}$ and $(\hat{a}_{ml})_{5\times5}$, and coefficient vectors $(\tilde{b}_1, ..., \tilde{b}_5)$ and $(\hat{b}_1, ..., \hat{b}_5)$, which can be represented by the following Butcher tableau

| | | | | | | | | | | | |
|---|---|---|---|---|---|---|---|---|---|---|---|
| | 0 | 0 | 0 | 0 | 0 | 0 | 0 | 0 | 0 | 0 | |
| | 0 | $\frac{1}{2}$ | 0 | 0 | 0 | $\frac{1}{2}$ | 0 | 0 | 0 | 0 | |
| $\tilde{a}_{ml}$ | 0 | $\frac{1}{6}$ | $\frac{1}{2}$ | 0 | 0 | $\frac{11}{18}$ | $\frac{1}{18}$ | 0 | 0 | 0 | $\hat{a}_{ml}$ |
| | 0 | $-\frac{1}{2}$ | $\frac{1}{2}$ | $\frac{1}{2}$ | 0 | $\frac{5}{6}$ | $-\frac{5}{6}$ | $\frac{1}{2}$ | 0 | 0 | |
| | 0 | $\frac{3}{2}$ | $-\frac{3}{2}$ | $\frac{1}{2}$ | $\frac{1}{2}$ | $\frac{1}{4}$ | $\frac{7}{4}$ | $\frac{3}{4}$ | $-\frac{7}{4}$ | 0 | |
| $\tilde{b}_l$ | 0 | $\frac{3}{2}$ | $-\frac{3}{2}$ | $\frac{1}{2}$ | $\frac{1}{2}$ | $\frac{1}{4}$ | $\frac{7}{4}$ | $\frac{3}{4}$ | $-\frac{7}{4}$ | 0 | $\hat{b}_l$ |

The left half of the tableau lists $\tilde{a}_{ml}$ and $\tilde{b}_l$, with the five rows from top to bottom referring to $m = 1, ..., 5$, and the columns from left to right referring to $l = 1, ..., 5$. Similarly, the right half lists $\hat{a}_{ml}$ and $\hat{b}_l$. We have also considered other high order IMEX methods, but we will not state them here to save space.

## 3.5 Linearized stability analysis

For simplicity, the resulting scheme is referred to as the "EIN-FD" scheme. Stability analysis of the EIN schemes with several different spatial discretization methods has been carried out

for the scalar diffusion equation in [34] and convection-diffusion equations in [32,33]. In this paper, stability would follow from the scalar results in [32, 33] if the inviscid and viscous Jacobian matrices are simultaneously diagonalizable. Unfortunately, these Jacobian matrices cannot be diagonalized simultaneously. It is necessary to conduct a separate stability analysis.

We attempt to give a stability analysis for the EIN-FD scheme for $\xi = x$, $\eta = y$ by the aid of the Fourier method. To apply Fourier analysis the scheme must be linearized first. We assume an initially undisturbed flow in which a small disturbance is introduced. Then the vector $\boldsymbol{U}$ is rewritten as the sum of the initial vector $\boldsymbol{U}_0 = [\rho_0, \rho_0 u_0, \rho_0 v_0, E_0]^\top$ (which is constant) and a perturbation vector $\tilde{\boldsymbol{U}}$

$$\boldsymbol{U} = \boldsymbol{U}_0 + \tilde{\boldsymbol{U}}. \tag{3.5}$$

Substituting (3.5) into the scheme and neglecting terms which are second order or higher in the perturbation variables, we then obtain a linearized EIN-FD scheme, which expresses the perturbation variables at a later time in terms of their current values.

To determine whether or not the scheme is linearly stable we substitute a test solution of the form

$$\tilde{\boldsymbol{U}}^n_{j,k} = \hat{\boldsymbol{U}}^n \exp[i(\omega_1 x_j + \omega_2 y_k)], \quad i^2 = -1$$

into the scheme. This leads to the following relationship

$$\hat{\boldsymbol{U}}^{n+1} = \boldsymbol{M}\hat{\boldsymbol{U}}^n,$$

where the amplification matrix $\boldsymbol{M}$ is $2\pi$-periodic in $z_1 = \omega_1 \Delta x$ and $z_2 = \omega_2 \Delta y$. Here, $\Delta x$ and $\Delta y$ represent the uniform mesh sizes along $x$- and $y$-directions, respectively. Given the values of variables other than $z_1$ and $z_2$, if $\boldsymbol{M}$ is uniformly diagonalizable and the spectral radius of $\boldsymbol{M}$ is not greater than 1 for all $z_1, z_2 \in [0, 2\pi)$, then the scheme is stable. A considerable amount of algebraic operations are required to analytically determine the eigenvalues of the matrix. For simplicity, we solve them numerically.

It is first noted that once the equation of state and values of $\boldsymbol{U}_0$, $\mu$ and $Pr$ are prescribed, the amplification matrix becomes a function of the five parameters $a_1$, $\frac{\Delta t}{\Delta x}$, $\frac{\Delta t}{\Delta y}$, $\frac{\Delta t}{\Delta x^2}$ and $\frac{\Delta t}{\Delta y^2}$. With the assumption of equal mesh spacing in the $x$- and $y$-directions we have $\lambda = \frac{\Delta t}{\Delta x} = \frac{\Delta t}{\Delta y}$ and $\nu = \frac{\Delta t}{\Delta x^2} = \frac{\Delta t}{\Delta y^2}$, and $\boldsymbol{M}$ is dependent upon $\lambda$, $\nu$ and $a_1$ only. It is of interest to explore the relationships of these parameters in greater detail. We will discuss in three different scenarios. First, when $a_1 = \nu = 0$, we would like to find the possible CFL-like stability condition that the scheme may be subject to. Second, when $\lambda = 0$, we would like to explore whether there are minimum and maximum values of $a_1$ such that the scheme is unconditionally stable. Finally, on the basis of these two cases, we analyze the stability of the full scheme.

When $a_1 = \nu = 0$, the amplification matrix $\boldsymbol{M}$ is a direct function of $\lambda$. Given, for example, the ideal gas EOS, the eigenvalues of $\boldsymbol{M}$ are computed with $u_0 = v_0 = 0$ and various different values of $\rho_0$ and $p_0$. We start with $\lambda = 0$ and examine whether the spectral radius of $\boldsymbol{M}$ is no greater than $1 + \epsilon$ for all sampled $\rho_0$, $p_0$, $z_1$ and $z_2$, where $\epsilon = 10^{-5}$ is used as a relaxation term. If yes, we increase the value of $\lambda$. Otherwise, we record the previous value as an estimate of the maximum value of $\lambda$. Finally, we find that the scheme is stable provided that

$$\lambda \leq C_u \min\left(\lambda_{c,1}^{\max} + \lambda_{c,2}^{\max}\right)^{-1}, \qquad C_u \leq 1.2, \tag{3.6}$$

where $\lambda_{c,1}^{\max}$ and $\lambda_{c,2}^{\max}$ are given by (2.8).

When $\lambda = 0$, the amplification matrix $\boldsymbol{M}$ is a direct function of $a_1$ and $\nu$. In this case, we would like to find the minimum and maximum values of $a_1$ such that the stability is independent of $\nu$. The minimum and maximum values of $a_1$ are obtained by following a similar reasoning as in the previous case. We find that regardless of the values of $\mu$ and $Pr$, the scheme is unconditionally stable provided that

$$a_1 = a_0 \times \lambda_{\mu}^{\max}, \qquad a_0 \geq 0.54, \tag{3.7}$$

where $\lambda_{\mu}^{\max}$ is given by (2.5).

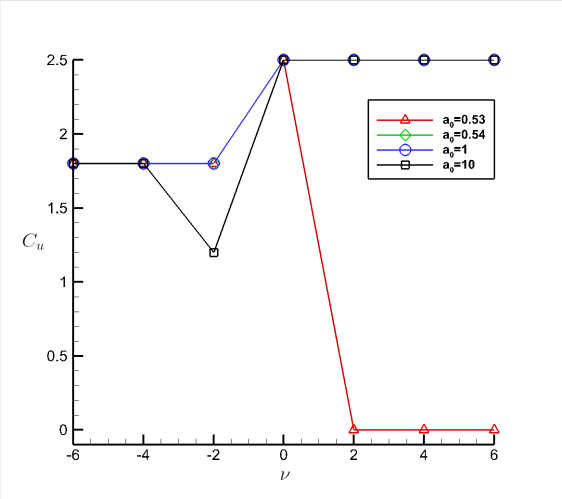


Figure 3.1: When $\mu = 1$ and $Pr = 0.75$, the maximum Courant number $C_u$ vs. $\nu$ for different values of $a_0$. $C_u$ is capped at 2.5.

On the basis of the above stability results, we then further analyze the stability of the full scheme. With the assumptions of $\lambda = C_u \min\left(\lambda_{c,1}^{\max} + \lambda_{c,2}^{\max}\right)^{-1}$, the stability of the full scheme is investigated. The result shows that regardless of the values of $\mu$ and $Pr$ the scheme can always be stable under the time step (3.6) provided that the condition (3.7) is satisfied. As an example, we take $\mu = 1$ and $Pr = 0.75$ and present the results in Figure 3.1, where the maximum Courant number $C_u$ vs. $\nu$ is plotted for various values of $a_0$.

We have also analyzed the stability of the scheme under the van der Waals EOS (2.7). The results indicate that the selection of the EOS will not change the stability results. We summarize the stability results of the scheme in the following proposition.

**Proposition 3.1.** *For the Navier-Stokes equations* (3.2) *with* $\xi = x$ *and* $\eta = y$*, whether considering the ideal gas EOS or the van der Waals EOS, to ensure the stability of the EIN-FD scheme with respect to small perturbations in free stream with velocities of 0, the following conditions should be satisfied*

$$\lambda \le C_u \min\left(\lambda_{c,1}^{\max} + \lambda_{c,2}^{\max}\right)^{-1}, \qquad C_u \le 1.2, \tag{3.8a}$$

$$a_1 = a_0 \times \lambda_{\mu}^{\max}, \qquad a_0 \ge 0.54, \tag{3.8b}$$

*where* $\lambda_{c,1}^{\max}$ *and* $\lambda_{c,2}^{\max}$ *are given by* (2.8)*, and* $\lambda_{\mu}^{\max}$ *is given by* (2.5)*.*

**Remark 3.1.** *We numerically find that the stability results are related to the initially undisturbed flow. However, when we set* $u_0 = v_0 = 0$*, the results are basically independent of* $\rho_0$ *and* $p_0$*. So in the analysis we specifically set* $u_0 = v_0 = 0$*. As stated in Proposition 3.1, the conditions* (3.8) *can only guarantee the stability of the EIN-FD scheme for free stream with velocities of 0. When the velocities of the flow are far from 0, the scheme may require a larger* $a_1$ *or a smaller time step to achieve stability. This is why the choice of the Courant number* $C_u$ *in the numerical experiment section depends on the considered problem.*

**Remark 3.2.** *The continuity equation in* (3.2) *does not contain second derivative. A natural idea is to directly use the explicit part of the IMEX method* (3.4) *to calculate the continuity equation without introducing the Laplacian terms on either side of the equation, i.e.,*

$$\frac{\partial J\boldsymbol{U}}{\partial t} + \underbrace{\frac{\partial \boldsymbol{G}_1}{\partial \xi} + \frac{\partial \boldsymbol{G}_2}{\partial \eta} - \frac{\partial \boldsymbol{G}_{\nu,1}}{\partial \xi} - \frac{\partial \boldsymbol{G}_{\nu,2}}{\partial \eta} + A_1\left(\frac{\partial^2 \boldsymbol{U}}{\partial \xi^2} + \frac{\partial^2 \boldsymbol{U}}{\partial \eta^2}\right)}_{\mathcal{T}_1} = \underbrace{A_1\left(\frac{\partial^2 \boldsymbol{U}}{\partial \xi^2} + \frac{\partial^2 \boldsymbol{U}}{\partial \eta^2}\right)}_{\mathcal{T}_2},$$

*where* $A_1 = \mathrm{diag}\{0, a_1, a_1, a_1\}$*. However, both the linear stability analysis and the numerical results show that the scheme obtained in this way is far less stable. To save space, the corresponding results will not be presented here.*

# 4 Numerical results

In this section, we will present several numerical examples to test the accuracy and the robustness of the EIN-FD scheme. In the computational results that follow, the order of accuracy is numerically calculated according to the following formula

$$\frac{\log(err_q(\Delta t_1)/err_q(\Delta t_2))}{\log(\Delta t_1/\Delta t_2)},$$

where $err_q(\Delta t_1)$ and $err_q(\Delta t_2)$ are the relative errors in the discrete $L^q$, $q \in \{1, 2, \infty\}$ norms. Here, $\Delta t_1$ and $\Delta t_2$ respectively refer to the minimum time step values for two

sets of successively refined computational meshes. The relative errors between the exact solution $U(x_j, y_k, t^n)$ and the numerical one $U^n_{j,k}$ are computed as follows

$$err_1 = \frac{\sum_{j=1}^{N_1}\sum_{k=1}^{N_2}|U(x_j,y_k,t^n) - U^n_{j,k}|}{\sum_{j=1}^{N_1}\sum_{k=1}^{N_2}|U(x_j,y_k,t^n)|},$$
$$err_2 = \frac{\sum_{j=1}^{N_1}\sum_{k=1}^{N_2}|U(x_j,y_k,t^n) - U^n_{j,k}|^2}{\sum_{j=1}^{N_1}\sum_{k=1}^{N_2}|U(x_j,y_k,t^n)|^2},$$
$$err_\infty = \frac{\max_{j,k}|U(x_j,y_k,t^n) - U^n_{j,k}|}{\max_{j,k}|U(x_j,y_k,t^n)|},$$

where $N_1$ and $N_2$ represent the number of grid points in the $x$- and $y$-directions, respectively.

In the previous section, we have provided the conditions for $a_1$ and $\Delta t$ to ensure that the EIN-FD scheme is linearly stable for small perturbations in free stream with velocities of 0. Based on the stability result we can provide a guidance for the choices of $a_1$ and $\Delta t$ to ensure the stability of the EIN-FD scheme in curvilinear coordinates for general computational fluid dynamics problems, i.e.,

$$a_1 = a_0 \times \lambda_\mu^{\max}, \qquad a_0 \geq 0.54,$$
$$\Delta t \leq C_u \min \frac{1}{J}\left[\frac{\lambda_{c,1}^{\max}}{\Delta\xi} + \frac{\lambda_{c,2}^{\max}}{\Delta\eta}\right]^{-1}, \qquad C_u \leq 1.2,$$

where $\lambda_{c,1}^{\max}$ and $\lambda_{c,2}^{\max}$ are given by (2.8), and $\lambda_\mu^{\max}$ is given by (2.5). All the following tests are run with $a_0 = 0.54$ but the choice of the Courant number $C_u$ depends on the considered problem.

## 4.1 1D viscous shockwave problem

We consider the classical one-dimensional viscous shockwave problem. It has an exact solution which was discovered by Becker [2] under the assumptions of steady state, one planar dimension, constant viscosity, an ideal gas equation of state, and a constant Prandtl number $Pr = 0.75$. The solution consists of implicit, closed-form expressions for the fluid variables and analytically captures the behaviour of shocks in ideal gases. In fact, we can directly use an IMEX method to solve the problem without iteratively solving nonlinear equations,

as the viscosity is constant. The reason for considering this problem is twofold. First, an analytical solution does exist which permits to compare the numerical results. Second, we would like to demonstrate the desired properties of the EIN-FD scheme in one dimension, such as high order accuracy and non-oscillation. The problem can perfectly meet our needs.

Let $\rho_l$ be the density at infinity on the left, $u_l$ be the velocity at infinity on the left and $u_r$ be the velocity at infinity on the right. We assume that $u_l > u_r$, $u_{lr} = \sqrt{u_l u_r}$. Since the solution is time-independent, the momentum is constant, say $m_1 = \rho_l u_l$. In the context of the above assumptions, it is shown in [2, 20] that the velocity profile is defined implicitly as the solution to the following equation

$$x = \frac{2}{\gamma+1}\frac{\kappa}{m_1 c_v}\int \frac{u}{(u-u_l)(u-u_r)}\mathrm{d}u. \tag{4.1}$$

The integral of (4.1) contains an additive constant consistent with the arbitrariness in the choice of the coordinate origin. Locating the origin at the point of inflection of the velocity profile, we then obtain

$$x = \frac{2}{\gamma+1}\frac{\kappa}{m_1 c_v}\left(\frac{u_l}{u_l-u_r}\log\left[\frac{u_l-u(x)}{u_l-u_{lr}}\right] - \frac{u_r}{u_l-u_r}\log\left[\frac{u(x)-u_r}{u_{lr}-u_r}\right]\right).$$

In order to obtain the desired velocity, we solve the equation numerically to high accuracy by the Newton's iteration. Once $u(x)$ is known, the density and the specific internal energy are given by

$$\rho(x) = \frac{m_1}{u(x)}, \qquad e(x) = \frac{1}{2\gamma}\left(\frac{\gamma+1}{\gamma-1}u_{lr}^2 - u^2(x)\right).$$

To obtain a time-dependent solution, which is computationally more challenging, we introduce a constant translation velocity $u_c$ and define

$$\boldsymbol{U} = \begin{pmatrix} \rho(x-u_c t) \\ \rho(x-u_c t)\big(u_c + u(x-u_c t)\big) \\ \rho(x-u_c t)\Big(e(x-u_c t) + \frac{1}{2}\big(u_c + u(x-u_c t)\big)^2\Big) \end{pmatrix}.$$

The field $\boldsymbol{U}$ with any $u_c$ constitutes an exact solution to the Navier-Stokes equations, since the equations are Galilean invariant. We remark that the solution is also used for instance in [13, 16] for convergence verification. In the test, we take $u_c = 0.2$, $u_l = 1$, $\rho_l = 1$. The

velocity $u_r$ is expressed in terms of both the pre-shock Mach number $M_a$ and $u_l$ via the Rankine-Hugoniot jump conditions

$$\frac{u_r}{u_l} = \frac{\gamma - 1 + 2M_a^{-2}}{\gamma + 1}.$$

We assume that the physical domain is truncated to $[-1.5, 1.5]$ and divided into $N$ equal parts. The flow variables at ghost points are fixed to the analytical solutions.

First, we take $M_a = 1.5$, $C_u = 1$ and $\mu = 0.01$. The simulations are run until $t_f = 5$, and the the distance traveled by the shock is 1. The results are reported in Table 4.1 where errors and orders are measured for the conserved variables. As expected, we can observe the optimal order of accuracy. Second, we take $M_a = 15$ and $\mu = 10^{-5}$, and show in Figure 4.1 the results obtained for velocity and temperature with 321 uniform mesh grids. As we can see, the numerical solutions are in good agreement with the exact ones.

Table 4.1: Accuracy test for the 1D viscous shockwave problem with the pre-shock Mach number $M_a = 1.5$ and the constant viscosity $\mu = 0.01$.

| variables | $N$ | $L^1$ error | order | $L^\infty$ error | order | $L^2$ error | order |
|---|---|---|---|---|---|---|---|
| Density | 80 | 1.190E-03 | | 1.235E-02 | | 4.032E-03 | |
| | 160 | 9.883E-05 | 3.590 | 1.998E-03 | 2.627 | 3.953E-04 | 3.351 |
| | 320 | 4.200E-06 | 4.556 | 1.035E-04 | 4.272 | 1.728E-05 | 4.516 |
| | 640 | 1.460E-07 | 4.846 | 2.976E-06 | 5.120 | 5.724E-07 | 4.916 |
| Momentum | 80 | 2.782E-04 | | 9.044E-03 | | 1.226E-03 | |
| | 160 | 3.003E-05 | 3.212 | 1.692E-03 | 2.419 | 1.691E-04 | 2.859 |
| | 320 | 1.287E-06 | 4.544 | 8.112E-05 | 4.382 | 8.080E-06 | 4.387 |
| | 640 | 4.256E-08 | 4.918 | 2.655E-06 | 4.933 | 2.448E-07 | 5.045 |
| Energy | 80 | 9.000E-04 | | 1.090E-02 | | 3.068E-03 | |
| | 160 | 7.189E-05 | 3.646 | 1.575E-03 | 2.791 | 2.889E-04 | 3.409 |
| | 320 | 3.086E-06 | 4.542 | 8.250E-05 | 4.255 | 1.291E-05 | 4.484 |
| | 640 | 1.079E-07 | 4.837 | 2.507E-06 | 5.040 | 4.348E-07 | 4.892 |

## 4.2 2D viscous shockwave problem

We use again the exact shockwave solution described in Section 4.1 to verify the error accuracy of the scheme in two-space dimensions. The convergence tests are done in the domain

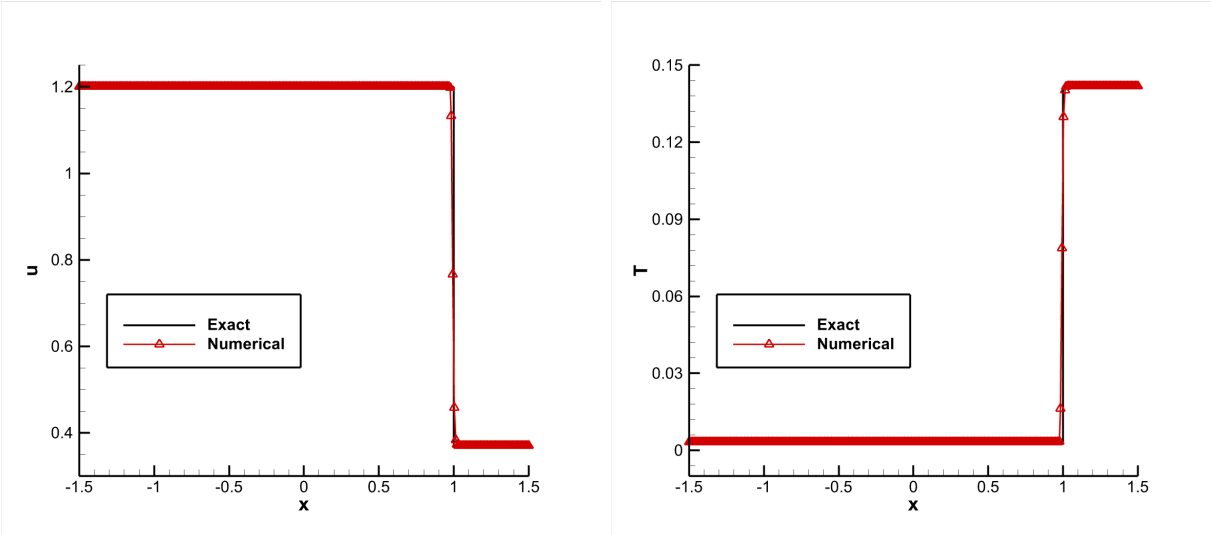


(a) velocity (b) temperature

Figure 4.1: 1D viscous shockwave problem with the pre-shock Mach number $M_a = 15$ and the viscosity coefficient $\mu = 10^{-5}$.

$(x, y) \in [-1.5, 1.5] \times [0, 1]$ with analytical boundary conditions on the left and right sides, and periodic boundary conditions in the vertical direction. The nonuniform nonorthogonal mesh

$$x = \xi + 0.05 \sin(2\pi\eta), \qquad y = \eta + 0.05 \sin\left(\frac{2}{3}\pi\xi\right) \tag{4.2}$$

is used to study the convergence behavior of our scheme. As in the previous problem, we take $M_a = 1.5$, $C_u = 1$, $\mu = 0.01$. The final time of the simulation is $t_f = 3$ and the test is run on a sequence of successively refined computational meshes. The results are reported in Table 4.2 where errors and orders are measured for the conserved variables. The scheme is proven to achieve the formal order of accuracy.

## 4.3 2D compressible Couette flow

The two-dimensional compressible Couette flow, which has an analytical solution, is also considered to test the performance of the scheme. The compressible Couette flow is a shear flow bounded by two parallel flat plates. The flow is driven by the moving upper plate

Table 4.2: Accuracy test for the 2D viscous shockwave problem on smooth meshes (4.2). $N_2 = N_1/3$.

| variables | $N_1$ | $L^1$ error | order | $L^\infty$ error | order | $L^2$ error | order |
|---|---|---|---|---|---|---|---|
| Density | 60 | 2.276E-03 | | 3.331E-02 | | 7.511E-03 | |
| | 120 | 2.957E-04 | 2.920 | 6.741E-03 | 2.286 | 1.093E-03 | 2.758 |
| | 180 | 5.735E-05 | 4.026 | 1.703E-03 | 3.377 | 2.367E-04 | 3.755 |
| | 240 | 1.537E-05 | 4.561 | 4.917E-04 | 4.303 | 6.529E-05 | 4.462 |
| Momentum | 60 | 6.545E-04 | | 1.894E-02 | | 2.455E-03 | |
| | 120 | 9.329E-05 | 2.787 | 4.377E-03 | 2.096 | 4.438E-04 | 2.447 |
| | 180 | 2.112E-05 | 3.646 | 1.399E-03 | 2.800 | 1.224E-04 | 3.162 |
| | 240 | 5.787E-06 | 4.485 | 4.124E-04 | 4.231 | 3.500E-05 | 4.338 |
| Energy | 60 | 1.764E-03 | | 2.672E-02 | | 5.832E-03 | |
| | 120 | 2.262E-04 | 2.938 | 5.511E-03 | 2.258 | 8.466E-04 | 2.761 |
| | 180 | 4.332E-05 | 4.057 | 1.358E-03 | 3.439 | 1.797E-04 | 3.805 |
| | 240 | 1.155E-05 | 4.578 | 3.914E-04 | 4.309 | 4.926E-05 | 4.483 |

at $y = 2H$, which has a constant speed $u_1$ in the horizontal direction and temperature $T_1 = 1$. The lower plate at $y = 0$ is stationary and adiabatic. We assume that the physical domain is truncated to be $(x, y) \in [0, 4H] \times [0, 2H]$ with $H = 1$. The Reynolds number is $Re = \rho_1 u_1 H/\mu_1 = 1$ with $\rho_1 = 1$, the Prandtl number is $Pr = 1$ and the gas constant in the ideal gas EOS is $R = \frac{1}{\gamma}$.

Assuming that the viscosity of the flow is determined by (2.3) with $\beta = 2$, $\mu_T = \mu_1$, $S_\mu = 0$ and $T_\mu = T_1$, an analytical solution for this steady flow [21] can be deduced as follows, in which the streamwise velocity, $u = u(y)$, satisfies a cubic equation and other variables can be obtained thereafter,

$$\left(1 + Pr\frac{\gamma-1}{3}M_a^2\right)\frac{y}{2H} = \frac{u}{u_1} + Pr\frac{\gamma-1}{2}M_a^2\left(\frac{u}{u_1} - \frac{u^3}{3u_1^3}\right),$$
$$\frac{T}{T_1} = 1 + Pr\frac{\gamma-1}{2}M_a^2\left(1 - \frac{u^2}{u_1^2}\right), \qquad v = 0, \qquad p = \frac{1}{\gamma},$$

where the Mach number is defined as $M_a = u_1/\sqrt{\gamma R T_1}$. We remark that this problem is also used for instance in [36] for accuracy verification. The difference is that the Reynolds number used in this paper is very small. The simulation is conducted for subsonic flow with

$M_a = 0.9$, $C_u = 1.2$ and the following initial conditions

$$u = v = 0, \quad T = 1, \quad p = \frac{1}{\gamma}.$$

In the test, the flow variables at ghost points are fixed to the analytical solutions for all boundaries. As in [36], the steady state is assumed to be achieved when the residual of the velocity is less than $2 \times 10^{-14}$. The errors and orders of the density, the horizontal velocity component and the temperature are presented in Table 4.3, from which we can clearly observe the designed orders of accuracy. Figure 4.2 shows the residuals on a sequence of successively refined meshes. As we can see, the scheme achieves nearly machine-zero convergence.

Table 4.3: Accuracy test for the 2D compressible Couette flow with $M_a = 0.9$.

| variables | $N_1 = N_2$ | $L^1$ error | order | $L^\infty$ error | order | $L^2$ error | order |
|---|---|---|---|---|---|---|---|
| Density | 20 | 4.502E-08 | | 1.476E-07 | | 5.159E-08 | |
| | 40 | 3.232E-09 | 3.726 | 1.244E-08 | 3.499 | 3.710E-09 | 3.724 |
| | 60 | 5.757E-10 | 4.511 | 2.342E-09 | 4.365 | 6.614E-10 | 4.508 |
| | 80 | 1.605E-10 | 4.655 | 6.697E-10 | 4.563 | 1.847E-10 | 4.649 |
| Velocity $u$ | 20 | 4.372E-09 | | 4.926E-09 | | 4.543E-09 | |
| | 40 | 3.245E-10 | 3.679 | 3.662E-10 | 3.677 | 3.402E-10 | 3.666 |
| | 60 | 5.789E-11 | 4.507 | 6.787E-11 | 4.407 | 6.158E-11 | 4.469 |
| | 80 | 1.613E-11 | 4.658 | 2.000E-11 | 4.454 | 1.748E-11 | 4.591 |
| Temperature | 20 | 4.708E-09 | | 8.463E-09 | | 5.299E-09 | |
| | 40 | 5.263E-10 | 3.100 | 9.791E-10 | 3.051 | 6.024E-10 | 3.076 |
| | 60 | 1.280E-10 | 3.697 | 2.411E-10 | 3.664 | 1.474E-10 | 3.681 |
| | 80 | 4.501E-11 | 3.809 | 8.534E-11 | 3.785 | 5.200E-11 | 3.797 |

## 4.4 2D manufactured problem

In this test, we consider the two-dimensional Navier-Stokes equations where the viscosity coefficient $\mu$ is determined by the Sutherland's law (2.3). This problem has an artificial exact solution that is obtained by balancing the Navier-Stokes equations with source terms on the right-hand side. The source terms can be easily computed using a computer algebra package. The exact solution of the problem in terms of primitive variables is defined to be

$$\rho = \rho_1 + \rho_2 \cos(x + y + t), \quad u = u_1 + u_2 \sin(x + y + t),$$

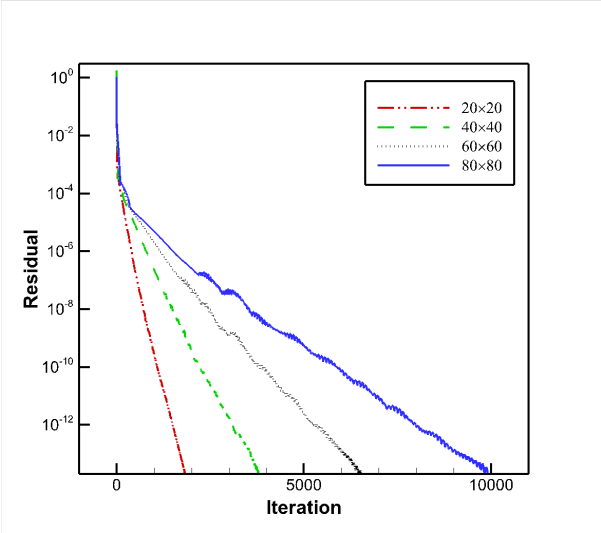


Figure 4.2: Convergence histories for the 2D compressible Couette flow with $M_a = 0.9$.

$$v = v_1 + v_2 \cos(x + y + t), \quad p = p_1 + p_2 \sin(x + y + t)$$

with the constants

$$\rho_1 = u_1 = v_1 = 1, \;\; p_1 = \frac{1}{\gamma}, \;\; \rho_2 = \frac{1}{2}, \;\; u_2 = v_2 = \frac{1}{4}, \;\; p_2 = \frac{1}{10}.$$

In addition to the ideal gas EOS (2.6), we also consider the van der Waals EOS (2.7) with $b_v = \frac{1}{3}$ in this test. We set the constants in the Sutherland's law (2.3) to

$$\mu_T = 0.1, \quad S_\mu = 1, \quad T_\mu = 1, \quad \beta = \frac{3}{2}.$$

The Prandtl number is fixed to $Pr = 0.75$, and the heat capacity at constant volume is chosen as $c_v = 1$. The computational domain is $[-\pi, \pi]^2$, and a nonuniform mesh is provided by the following coordinate transformation

$$x = \xi + 0.1 \sin(\eta) \sin(\xi), \qquad y = \eta + 0.1 \cos(\xi) \cos(\eta). \tag{4.3}$$

The Courant number is $C_u = 1.2$ and the final time of the simulation is $t_f = \pi$. We present the results for these two different equations of state in Tables 4.4 and 4.5, respectively. In both tables, the errors and orders are measured in $L^1$, $L^2$ and $L^\infty$ norms for the density $\rho$,

the momentum $\rho\sqrt{u^2+v^2}$ and the energy $E$. As we can see, no matter which equation of state is considered, the scheme can achieve the designed order of accuracy.

In order to illustrate the high efficiency of the EIN-FD scheme, the third order strong stability-preserving (SSP) Runge-Kutta method [29] combined with the spatial discretizations considered in this paper has also been taken into account. For simplicity, this purely explicit scheme is referred to as the "SSPRK-FD" scheme. As an explicit discretization of the viscous terms is forwarded, from the numerical viewpoint, the SSPRK-FD scheme is responsible for a parabolic time step restriction that writes

$$\Delta t \leq C_u^* \min \frac{1}{J}\left[\frac{\lambda_{c,1}^{\max}}{\Delta\xi}+\frac{\lambda_{c,2}^{\max}}{\Delta\eta}+\lambda_{\mu}^{\max}\left(\frac{1}{\Delta\xi^2}+\frac{1}{\Delta\eta^2}\right)\right]^{-1},$$

where $C_u^*$ is chosen as 0.5 in this paper, $\lambda_{c,1}^{\max}$ and $\lambda_{c,2}^{\max}$ are given by (2.8), and $\lambda_{\mu}^{\max}$ is given by (2.5). The time step restriction might become very severe for high viscosity coefficients and small mesh sizes. We compare the computational costs required for the SSPRK-FD and EIN-FD schemes. When evaluating the computational cost, the simulation is carried out with the Intel Core i7-4790 CPU @ 3.60 GHz. The source code used here is written in Fortran 90 and has not been parallelized. The linear system is solved with the PARDISO routine. When $N_1 = N_2 = 160$ and $t_f = 0.1$, we show in Table 4.6 the CPU time required for this problem with different viscosity coefficient $\mu_T$. For the same viscosity coefficient $\mu_T = 0.5$, the computational cost of the schemes at different grid sizes is compared in Table 4.7. As we can see, for high viscosity coefficients or small mesh sizes, the CPU time required by the EIN-FD scheme is much lower than the one required by the SSPRK-FD scheme.

## 4.5 The first Stokes problem

In this test, the first Stokes problem is selected to validate the robustness and accuracy of our scheme in the presence of highly stretched meshes and rather low Mach number. Previous calculations of the problem can also be found in [6, 13]. The test case studies the motion of the fluid above and below an infinite plate which is suddenly decelerated to zero velocity.

Table 4.4: Accuracy test for the 2D artificial example on smooth meshes (4.3). The ideal gas EOS (2.6) is considered.

| variables | $N_1 = N_2$ | $L^1$ error | order | $L^\infty$ error | order | $L^2$ error | order |
|---|---|---|---|---|---|---|---|
| Density | 20 | 3.906E-04 | | 8.901E-04 | | 4.553E-04 | |
| | 40 | 2.563E-05 | 3.926 | 8.594E-05 | 3.369 | 3.372E-05 | 3.751 |
| | 80 | 2.566E-06 | 3.319 | 6.283E-06 | 3.773 | 3.203E-06 | 3.395 |
| | 160 | 3.579E-07 | 2.842 | 7.860E-07 | 2.999 | 4.272E-07 | 2.906 |
| Momentum | 20 | 5.488E-04 | | 1.214E-03 | | 6.289E-04 | |
| | 40 | 3.504E-05 | 3.965 | 7.639E-05 | 3.986 | 3.947E-05 | 3.990 |
| | 80 | 3.513E-06 | 3.317 | 5.365E-06 | 3.831 | 3.708E-06 | 3.411 |
| | 160 | 4.522E-07 | 2.958 | 6.539E-07 | 3.036 | 4.687E-07 | 2.984 |
| Energy | 20 | 4.640E-04 | | 1.030E-03 | | 5.399E-04 | |
| | 40 | 4.181E-05 | 3.468 | 1.024E-04 | 3.327 | 4.968E-05 | 3.438 |
| | 80 | 4.861E-06 | 3.104 | 1.392E-05 | 2.878 | 5.914E-06 | 3.070 |
| | 160 | 6.308E-07 | 2.946 | 1.928E-06 | 2.851 | 7.893E-07 | 2.905 |

Table 4.5: Accuracy test for the 2D artificial example on smooth meshes (4.3). The van der Waals EOS (2.7) with $b_v = \frac{1}{3}$ is considered.

| variables | $N_1 = N_2$ | $L^1$ error | order | $L^\infty$ error | order | $L^2$ error | order |
|---|---|---|---|---|---|---|---|
| Density | 20 | 3.933E-04 | | 9.743E-04 | | 4.657E-04 | |
| | 40 | 2.081E-05 | 4.239 | 6.361E-05 | 3.936 | 2.815E-05 | 4.047 |
| | 80 | 2.147E-06 | 3.267 | 5.377E-06 | 3.553 | 2.690E-06 | 3.377 |
| | 160 | 2.994E-07 | 2.842 | 6.345E-07 | 3.083 | 3.557E-07 | 2.919 |
| Momentum | 20 | 4.596E-04 | | 9.839E-04 | | 5.301E-04 | |
| | 40 | 2.390E-05 | 4.264 | 4.547E-05 | 4.434 | 2.686E-05 | 4.302 |
| | 80 | 2.471E-06 | 3.264 | 4.304E-06 | 3.391 | 2.702E-06 | 3.303 |
| | 160 | 3.121E-07 | 2.985 | 5.217E-07 | 3.044 | 3.430E-07 | 2.977 |
| Energy | 20 | 4.408E-04 | | 1.007E-03 | | 5.312E-04 | |
| | 40 | 3.507E-05 | 3.651 | 9.509E-05 | 3.404 | 4.402E-05 | 3.592 |
| | 80 | 3.963E-06 | 3.136 | 1.338E-05 | 2.820 | 5.204E-06 | 3.071 |
| | 160 | 4.987E-07 | 2.990 | 1.765E-06 | 2.922 | 6.807E-07 | 2.934 |

Table 4.6: Comparison of the CPU time between the EIN-FD and SSPRK-FD schemes for the 2D manufactured problem with different viscosity coefficient $\mu_T$. The simulations are run on the smooth mesh (4.3) with $160 \times 160$ mesh grids until $t_f = 0.1$.

| $\mu_T$ | EIN-FD | SSPRK-FD | ratio |
|---|---|---|---|
| 0.1 | 69 | 106 | 1.54 |
| 0.5 | | 502 | 7.28 |
| 1 | | 1015 | 14.71 |

Table 4.7: Comparison of the CPU time between the EIN-FD and SSPRK-FD schemes for the 2D manufactured problem with $\mu_T = 0.5$. The simulations are run on the smooth mesh (4.3) with $N_1 \times N_2$ mesh grids until $t_f = 0.1$.

| $N_1 = N_2$ | EIN-FD | SSPRK-FD | ratio |
|---|---|---|---|
| 160 | 69 | 502 | 7.28 |
| 240 | 200 | 2668 | 13.34 |
| 320 | 459 | 8901 | 19.39 |

Let the plate be at $y = 0$. The fluid above and below the plate initially moves uniformly at opposite horizontal velocities and has the following initial state

$$v = 0, \quad u = \begin{cases} u_0, & y \geq 0 \\ -u_0, & y < 0 \end{cases}, \quad u_0 = 1, \quad \rho = 1, \quad p = \frac{100}{\gamma}.$$

Assuming that the plate suddenly stops at $t = 0$, an analytical solution is available considering the incompressible Navier-Stokes equations, which writes the velocity component $u$ as

$$u(y,t) = u_0 \operatorname{erf}\left(\frac{y}{2\sqrt{\mu t/\rho}}\right),$$

where

$$\operatorname{erf}(\xi_0) = \frac{2}{\sqrt{\pi}} \int_0^{\xi_0} \exp(-\xi^2)\, \mathrm{d}\xi.$$

The simulation is run at a rather low Mach number of $M_a = 0.1$, it therefore constitutes a useful test case for compressible Navier-Stokes solvers.

We choose a constant viscosity $\mu = 0.1$ and the Prandtl number is set to $Pr = 1$. The ideal gas EOS with $R = \frac{1}{\gamma}$ is considered. In order to get fine solutions near the plate, numerically the grid is equally spaced in the $x$-direction and continuously stretched in the $y$-direction, using the mapping

$$x = \xi, \qquad y = \frac{L_y}{2} \frac{\sinh(\sigma_y \eta)}{\sinh(\sigma_y)}, \tag{4.4}$$

where $L_y$ is taken as 4 and $\sigma_y = 5$ is a stretching factor. Simulations of this test are performed in the computational domain $[-\frac{1}{2}, \frac{1}{2}] \times [-1, 1]$ with $21 \times 81$ uniform meshes. Via the mapping

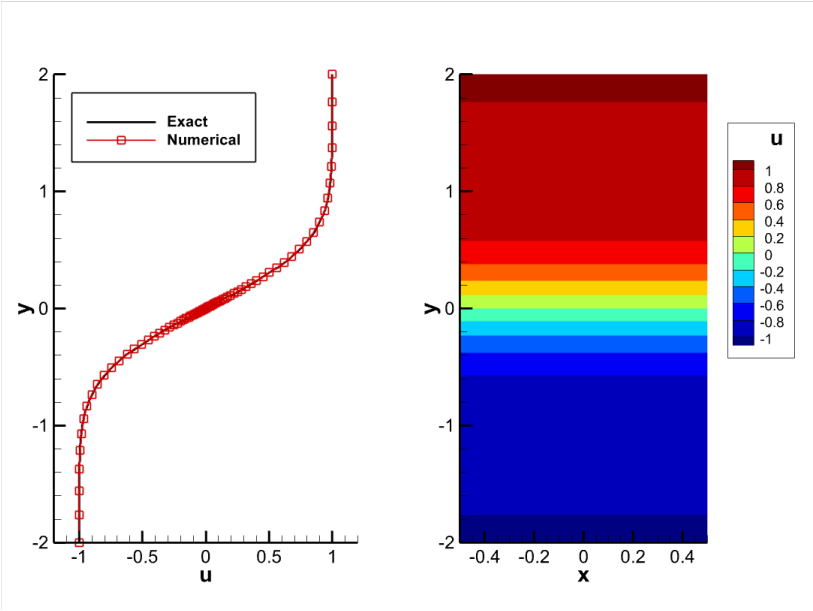


Figure 4.3: The velocity distribution at $t_f = 1$ for the first Stokes problem. Left: comparison of the horizontal velocity component and exact solution along the $y$-direction at $x = 0$. Right: 2D view of the computational domain with horizontal velocity contours. 11 uniform contours from -1 to 1 are shown.

(4.4), the ratio of the largest mesh spacing along the $y$-direction to the smallest one is about 69.6. Periodic boundary condition is applied in the horizontal direction, whereas the freestream values are imposed at the lower and upper boundaries. The comparison between the analytical solution and our numerical solution at $t_f = 1$ is presented in Figure 4.3. In this test, the simulation is run with $C_u = 1.2$. We can notice the good agreement between the numerical result and the exact one.

## 4.6 2D viscous shock tube problem

In this test we consider a high-speed viscous flow. The flow is bounded by a unit square $[0, 1]^2$ with a diaphragm at $x = \frac{1}{2}$ separating it in two parts. The fluid is initially at rest and the initial state is

$$(\rho, u, v, p) = \begin{cases} \left(120, 0, 0, \frac{120}{\gamma}\right), & 0 \leq x \leq 0.5, \\ \left(1.2, 0, 0, \frac{1.2}{\gamma}\right), & 0.5 \leq x \leq 1, \end{cases}$$

with $\gamma = 1.4$. The Prandtl number is $Pr = 0.73$. No-slip adiabatic conditions are applied at all boundaries of the square. At time zero the diaphragm is broken and then the solution will develop complex two-dimensional shock/shear/boundary-layer interactions. The flow contains structures of various length scales, making it an ideal test case for evaluating high-resolution schemes. Next, we will conduct testing in two scenarios.

### 4.6.1 Constant viscosity and the ideal gas EOS

We first consider the flow with constant viscosity $\mu = 0.005$ and the ideal gas equation of state. The corresponding Reynolds number is 200. Previous calculations of the problem can be found in [9, 37] and the references therein, so it is of interest to have a comparison. To avoid complex technicalities regarding boundary treatments, we extrapolate the interior values and the boundary conditions to the ghost nodes outside the computational domain using symmetry / anti-symmetry. Specifically, across a line of symmetry, $\rho$ and $E$ are reflected symmetrically while $\rho u$ and $\rho v$ are reflected anti-symmetrically. We show in Figure 4.4(a) the density contours at $t_f = 1$ on uniform mesh with $401 \times 401$ mesh grids. Due to the high cost of computing, to safeguard against numerous tests for optimal CFL for this problem, a conservative CFL of $C_u = 0.1$ is used. Since the solution is symmetric about the line $y = 0.5$, to enhance viewing, the enlarged view of the density contours is shown in Figure 4.4(b), where the plotting region concentrates only on $0.4 \leq x \leq 1$, $0 \leq y \leq 0.4$. Clearly, the complex flow structures are well captured by the scheme and they agree well with the results reported in [9, 37], demonstrating the good performance of the scheme in high-speed viscous flows. The density distribution along the bottom wall is presented in Figure 4.5. Several critical points extracted from the results of the high order gas-kinetic scheme [37] are used as the reference to quantitatively assess the performance of the EIN-FD scheme. In [37], a uniform mesh with $1500 \times 750$ cells is used in the lower half square. It can be observed that the result of our scheme is close to the reference data.

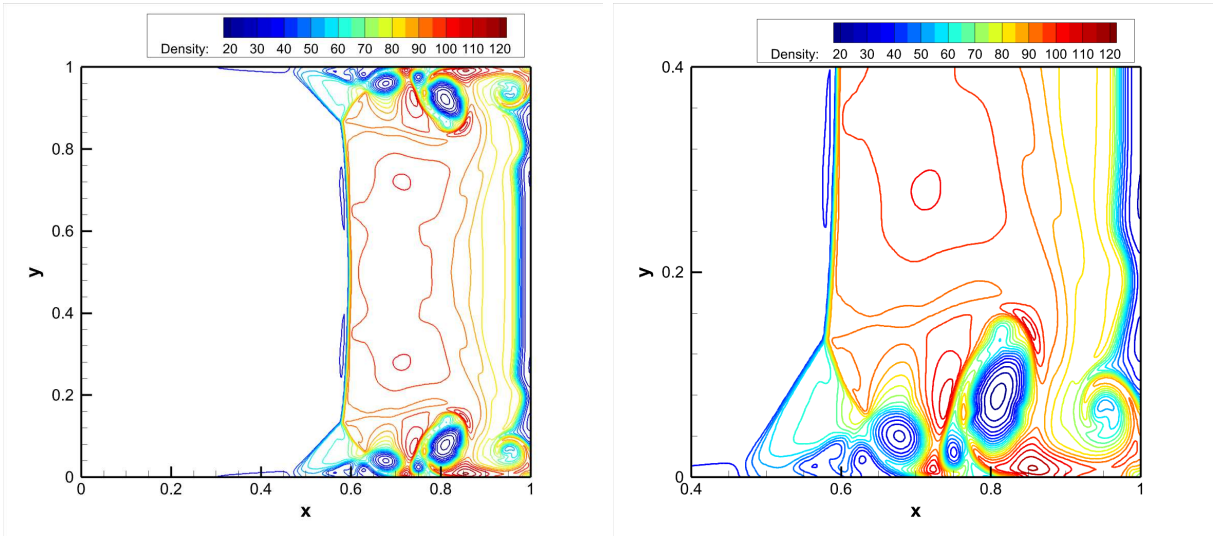


(a) full view (b) enlarged view

Figure 4.4: Density contours at $t_f = 1$ in the 2D viscous shock tube flow with $\mu = 0.005$ and the ideal gas EOS. 21 uniform contours from 20 to 120. Uniform mesh with $401 \times 401$ mesh grids in $[0, 1]^2$.

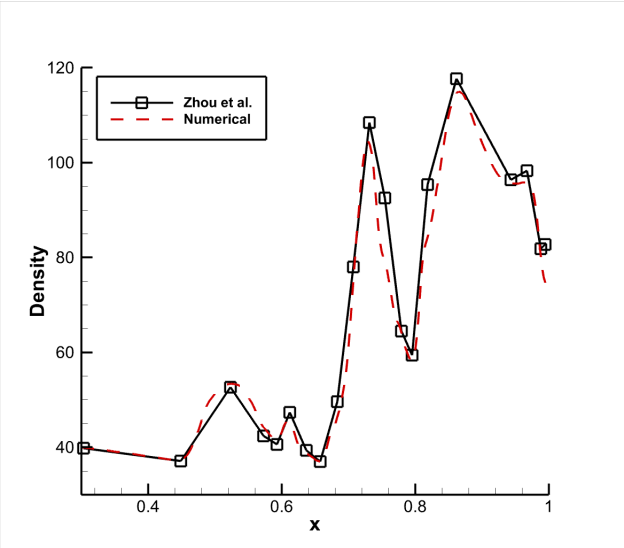


Figure 4.5: 2D viscous shock tube problem with $\mu = 0.005$ and the ideal gas EOS. Density distributions along the bottom wall at $t_f = 1$.

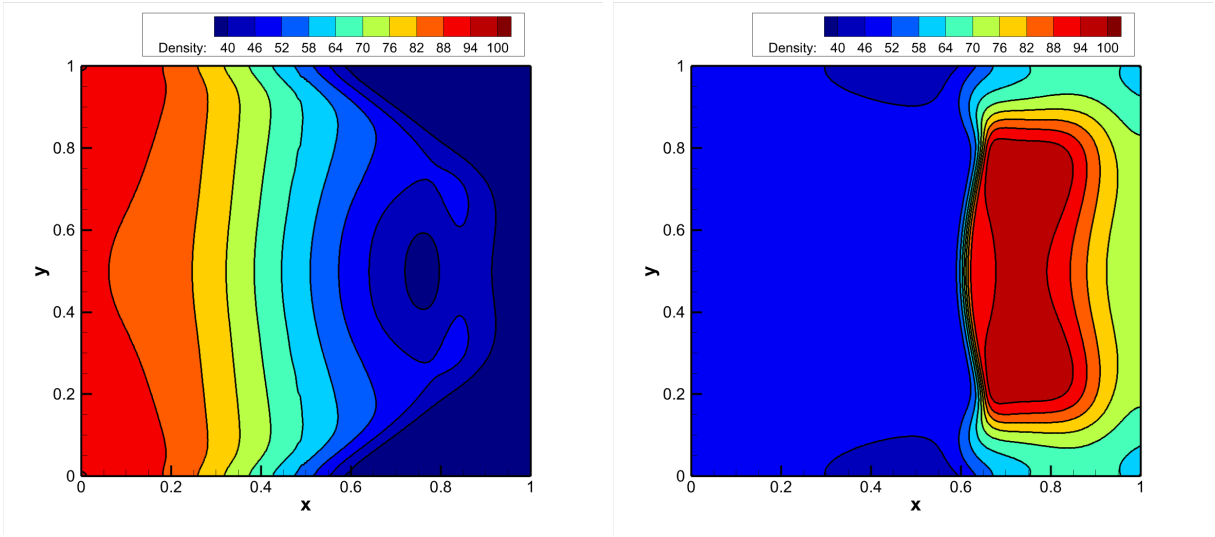


(a) $t_f = 0.5$ (b) $t_f = 1$

Figure 4.6: Density contours of the 2D viscous shock tube flow with the van der Waals EOS. 11 uniform contours from 40 to 100. Uniform mesh with $401 \times 401$ mesh grids in $[0, 1]^2$.

### 4.6.2 Nonlinear viscosity and the van der Waals EOS

We consider the van der Waals EOS (2.7) with $b_v = \frac{1}{480}$ this time. In addition, we assume that the viscosity coefficient $\mu$ is determined by the Sutherland's law (2.3) with

$$\mu_T = 1, \quad \beta = \frac{3}{2}, \quad T_\mu = 1, \quad S_\mu = \frac{1}{2}.$$

Since the viscous effects play an important relevant role, we take $C_u = 1.2$. The treatments of the boundary conditions remain consistent with the previous test. In addition, the simulation is run again on a uniform mesh with $401 \times 401$ mesh grids in the domain $[0, 1]^2$. We show in Figure 4.6 the density contours at $t_f = 0.5$ and $t_f = 1$. Although no exact and reference solutions are known, the analysis of the results can be qualitatively performed taking into account the symmetry of the flow structures and the features of the interactions. Overall, the main flow features are consistent with what we expect.

## 4.7 Time-developing mixing layer

In this test, we study vortex growth and pairing in a time-developing compressible mixing layer when the convective Mach number is equal to 0.8. At this convective Mach number the flow develops shock waves around the large-scale vortical structures [35], and the problem is to compute accurately the vortex evolution while avoiding oscillations around the shocks. The initial conditions consist of a parallel mean flow with a hyperbolic tangent profile plus perturbations of the velocity components. The mean profile of the velocity is specified by the relations

$$u = \frac{1}{2}(u_1 - u_2)\tanh(2y), \qquad v = 0.$$

Here subscripts 1 and 2 refer to the upper ($y > 0$) and lower ($y < 0$) streams of fluid, respectively. In the present computation $u_1 = -u_2 = 0.5$ are used. The pressure is assumed uniform initially. Then the normalized density and the local sound speed $c_s$ is determined from an assumption of constant stagnation enthalpy

$$c_s^2 = c_{s,1}^2 + \frac{\gamma - 1}{2}(u_1^2 - u^2).$$

The convective Mach number is defined by

$$M_c = \frac{u_1 - u_2}{c_{s,1} + c_{s,2}}.$$

The ideal gas EOS is considered and the Prandtl number is set to 1. The initial mean flow is unstable to small perturbations. The instability is forced, by adding small perturbations to the velocity components in the form of simple waves. The normal component of velocity is perturbed by a single mode, see [7],

$$\tilde{v} = 0.05 \exp\left(-\frac{y^2}{10}\right) \cos\left(\frac{4\pi x}{L_x} - \frac{\pi}{2}\right),$$

where $L_x = 30$ is the domain length in the $x$-direction. The perturbation in the streamwise velocity is found by assuming that the total perturbation is divergence free. The extent of the mixing layer is characterized through its vorticity thickness, defined as

$$\delta_\omega = \frac{u_1 - u_2}{\left(\frac{\mathrm{d}u}{\mathrm{d}y}\right)_{\max}}.$$

The initial vorticity thickness is used to define a Reynolds number as

$$Re = \frac{\rho_1 u_1 \delta_\omega(0)}{\mu_1},$$

where $\mu_1$ is the dynamic viscosity associated with the freestream of velocity $u_1$. In this test, we take $Re = 400$. Following [25], the dynamic viscosity is assumed to be given by the Sutherland's law

$$\mu/\mu_1 = \frac{(c_s^2/c_{s,1}^2)^{1.5}(1 + 110.3/300)}{c_s^2/c_{s,1}^2 + 110.3/300}.$$

The flow is periodic in the $x$-direction, so periodic boundary conditions are specified. Slip adiabatic wall conditions are imposed in the normal direction. Numerically the grid is equally spaced in the $x$-direction and stretched in the $y$-direction, using the mapping (4.4) with the box length in the $y$-direction $L_y = 100$ and the stretching factor $\sigma_y = 3$. The mapped coordinate $\eta$ is equally spaced and runs from $-1$ to 1. A refinement study for three different meshes ($101 \times 201$, $201 \times 401$ and $301 \times 601$) is carried out. A CFL number of 1.2 is used for all computations. We shown in Figure 4.7 the normalized vorticity thickness as a function of the non-dimensional time $t^* = u_1 t/\delta_\omega(0)$ and grid resolution. The grid-refinement study indicates that the solution obtained with our scheme is converged. Figure 4.8 shows the vorticity contours of the mixing layer on a mesh with $301 \times 601$ mesh grids at the dimensionless times $t^* = \{0, 10, 20, 30\}$. The vortex growth and pairing generated by the instability of the mixing layer can be seen clearly.

# 5 Conclusions

A high order finite difference scheme with the EIN time-marching method has been discussed for the compressible Navier-Stokes equations. Both the ideal gas and non-ideal gas equations of state are considered in this paper. Since we are mainly interested in time scales where viscous effects play an important relevant role, the EIN method is obtained by adding and subtracting a linear Laplacian term at one side of the system, and then treat one of these two terms implicitly and all the remaining terms explicitly. Thanks to the design, the viscous

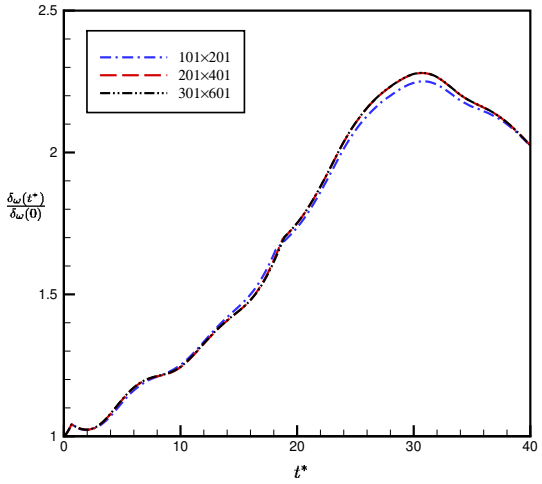


Figure 4.7: Variation of the normalized vorticity thickness with non-dimensional time $t^* = u_1 t/\delta_\omega(0)$ for the time-developing mixing layer.

terms in the CNS equations are advanced explicitly and the EIN method can achieve a more relaxed time step restriction than fully explicit methods. We have presented a linearized stability analysis of the EIN-FD scheme for free stream with velocities of 0. The stability result provides a guidance for the choices of $a_1$ and the time step to ensure the stability of the scheme. Numerical results indicate that the scheme is non-oscillatory and able to deliver the designed third order accuracy, while requiring remarkably less CPU time than the third order SSP Runge-Kutta method [29] for computing problems where nonlinear viscosity dominates. A main drawback of the finite difference scheme is that we need a considerable effort to generate a block-structured, body-fitted mesh for some problems. High resolution shock-capturing discontinuous Galerkin finite element methods do not have this intrinsic limitation. Coupled with the EIN time-marching method, more studies on the discontinuous Galerkin finite element methods constitute our future work.

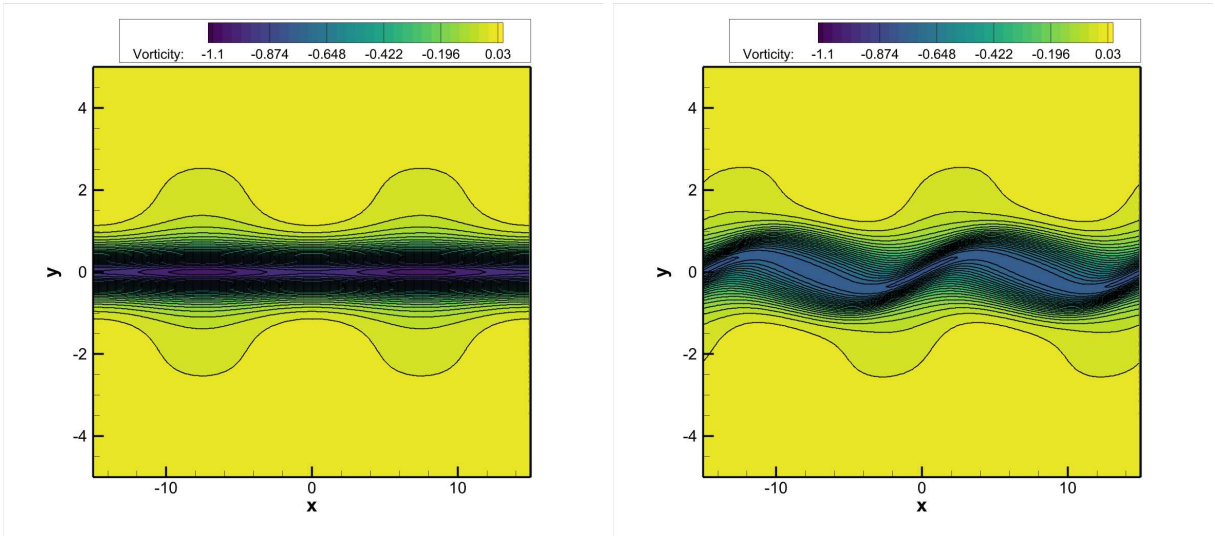


(a) $t^* = 0$ (b) $t^* = 10$

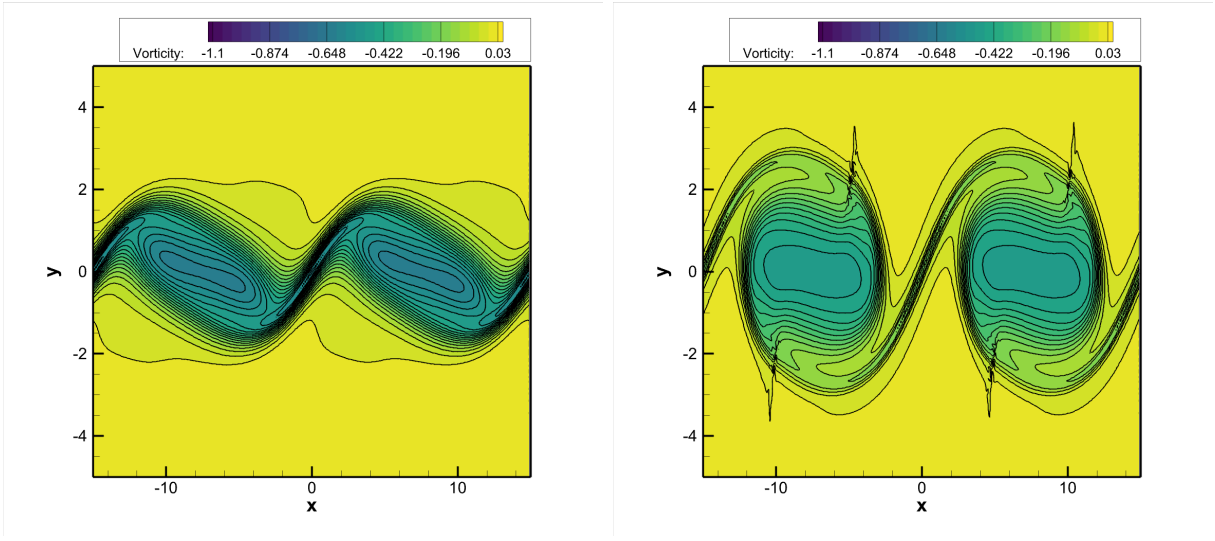


(c) $t^* = 20$ (d) $t^* = 30$

Figure 4.8: Vorticity contours of the time-developing mixing layer at the dimensionless times $t^* = u_1 t/\delta_\omega(0) = \{0, 10, 20, 30\}$. 31 equispaced contour levels from -1.1 to 0.03 are shown.

# References


[1] U. M. Ascher, S. J. Ruuth and R. J. Spiteri, *Implicit-explicit Runge-Kutta methods for time-dependent partial differential equations*, Applied Numerical Mathematics, 25, 1997, 151-167.

[2] R. Becker, *Stosswelle und detonation*, Physik, 8, 1923, 321-362.

[3] S. Boscarino, F. Filbet and G. Russo, *High order semi-implicit schemes for time dependent partial differential equations*, Journal of Scientific Computing, 68, 2016, 975-1001.

[4] W. Boscheri, G. Dimarco and M. Tavelli, *An efficient second order all Mach finite volume solver for the compressible Navier-Stokes equations*, Computer Methods in Applied Mechanics and Engineering, 374, 2021, 113602.

[5] W. Boscheri and L. Pareschi, *High order pressure-based semi-implicit IMEX schemes for the 3D Navier-Stokes equations at all Mach numbers*, Journal of Computational Physics, 434, 2021, 110206.

[6] W. Boscheri and M. Tavelli, *High order semi-implicit schemes for viscous compressible flows in 3D*, Applied Mathematics and Computation, 434, 2022, 127457.

[7] J. Chao, A. Haselbacher and S. Balachandar, *A massively parallel multi-block hybrid compact-WENO scheme for compressible flows*, Journal of Computational Physics, 228, 2009, 7473-7491.

[8] F. Cordier, P. Degond and A. Kumbaro, *An asymptotic-preserving all speed scheme for the Euler and Navier-Stokes equations*, Journal of Computational Physics, 231, 2012, 5685-5704.

[9] V. Daru and C. Tenaud, *Numerical simulation of the viscous shock tube problem by using a high resolution monotonicity-preserving scheme*, Computers & Fluids, 38, 2009, 664-676.

[10] P. Degond and M. Tang, *All speed scheme for the low mach number limit of the isentropic Euler equation*, Communications in Computational Physics, 10, 2011, 1-31.

[11] J. Douglas Jr. and T. Dupont, *Alternating-direction Galerkin methods on rectangles*, In: Numerical Solution of Partial Differential Equations-II, B. Hubbard (Ed), pp. 133-214, Academic Press (1971).

[12] L. Duchemin and J. Eggers, *The explicit-implicit-null method: Removing the numerical instability of PDEs*, Journal of Computational Physics, 263, 2014, 37-52.

[13] M. Dumbser, *Arbitrary high order PNPM schemes on unstructured meshes for the compressible Navier-Stokes equations*, Computers & Fluids, 39, 2010, 60-76.

[14] F. X. Giraldo, M. Restelli and M. Läuter, *Semi-implicit formulations of the Navier-Stokes equations: application to nonhydrostatic atmospheric modeling*, SIAM Journal on Scientific Computing, 32, 2010, 3394-3425.

[15] P. Glaister, *A shock-capturing scheme for body-fitted meshes*, International Journal for Numerical Methods in Fluids, 8, 1988, 1095-1105.

[16] J.-L. Guermond, M. Maiera, B. Popova and I. Tomas, *Second-order invariant domain preserving approximation of the compressible Navier-Stokes equations*, Computer Methods in Applied Mechanics and Engineering, 375, 2021, 113608.

[17] J. Haack, S. Jin and J.-G. Liu, *An all-speed asymptotic-preserving method for the isentropic Euler and Navier-Stokes equations*, Communications in Computational Physics, 12, 2012, 955-980.

[18] Douglas S. Harned and W. Kerner, *Semi-implicit method for three-dimensional compressible magnetohydrodynamic simulation*, Journal of Computational Physics, 60, 1985, 62-75.

[19] G. Jiang and C.-W. Shu, *Efficient implementation of weighted ENO schemes*, Journal of Computational Physics, 126, 1996, 202-228.

[20] B. M. Johnson, *Analytical shock solutions at large and small Prandtl number*, Journal of Fluid Mechanics, 726, 2013, R4, 12.

[21] H. W. Liepmann and A. Roshko, *Elements of Gasdynamics*, Wiley, New York, 1957.

[22] G. Orlando, P. F. Barbante and L. Bonaventura, *An efficient IMEX-DG solver for the compressible Navier-Stokes equations for non-ideal gases*, Journal of Computational Physics, 471, 2022, 111653.

[23] F. Renac, S. Gérald, C. Marmignon and F. Coquel, *Fast time implicit-explicit discontinuous Galerkin method for the compressible Navier-Stokes equations*, Journal of Computational Physics, 251, 2013, 272-291.

[24] M. Restelli and F. X. Giraldo, *A conservative discontinuous Galerkin semi-implicit formulation for the Navier-Stokes equations in nonhydrostatic mesoscale modeling*, SIAM Journal on Scientific Computing, 31, 2009, 2231-2257.

[25] N. D. Sandham and H. C. Yee, *A numerical study of a class of TVD schemes for compressible mixing layers*, NASA TM-102194, 1989.

[26] H. Shi and Y. Li, *Local discontinuous Galerkin methods with implicit-explicit multistep time-marching for solving the nonlinear Cahn-Hilliard equation*, Journal of Computational Physics, 394, 2019, 719-731.

[27] M. Shoeybi, M. Svärd, F. E. Ham and P. Moin, *An adaptive implicit-explicit scheme for the DNS and LES of compressible flows on unstructured grids*, Journal of Computational Physics, 229, 2010, 5944-5965.

[28] C.-W. Shu, *Essentially non-oscillatory and weighted essentially non-oscillatory schemes for hyperbolic conservation laws*, in *Advanced Numerical Approximation of Nonlinear*

*Hyperbolic Equations*, B. Cockburn, C. Johnson, C.-W. Shu and E. Tadmor (Editor: A. Quarteroni), Lecture Notes in Mathematics, volume 1697, Springer, Berlin, 1998, pp.325-432.

[29] C.-W. Shu and S. Osher,*Efficient implementation of essentially non-oscillatory shock-capturing schemes*, Journal of Computational Physics, 77, 1988, 439-471.

[30] P. Smereka, *Semi-Implicit level set methods for curvature and surface diffusion motion*, Journal of Scientific Computing, 19, 2003, 439-456.

[31] R. Span, *Multiparameter Equations of State*, Springer, 2000.

[32] M. Tan, J. Cheng and C.-W. Shu, *Stability of high order finite difference and local discontinuous Galerkin schemes with explicit-implicit-null time-marching for high order dissipative and dispersive equations*, Journal of Computational Physics, 464, 2022, 111314.

[33] M. Tan, J. Cheng and C.-W. Shu, *Stability of spectral collocation schemes with explicit-implicit-null time-marching for convection-diffusion and convection-dispersion equations*, East Asian Journal on Applied Mathematics, 13, 2023, 464-498.

[34] H. Wang, Q. Zhang, S. Wang and C.-W. Shu, *Local discontinuous Galerkin methods with explicit-implicit-null time discretizations for solving nonlinear diffusion problems*, Science China Mathematics, 63, 2020, 183-204.

[35] H. C. Yee, N. D. Sandham and M. J. Djomehri, *Low-dissipative high-order shock-capturing methods using characteristic-based filters*, Journal of Computational Physics, 150, 1999, 199-238.

[36] C. Zhang, Q. Li, S. Fu and Z. Wang, *A third-order gas-kinetic CPR method for the Euler and Navier-Stokes equations on triangular meshes*, Journal of Computational Physics, 363, 2018, 329-353.

[37] G. Zhou, K. Xu and F. Liu, *Grid-converged solution and analysis of the unsteady viscous flow in a two-dimensional shock tube*, Physics of Fluids, 30, 2018, 016102.

# Appendix

## The Roe-type characteristic decomposition matrix $\boldsymbol{A}_{j+\frac{1}{2},k}$

We assume that $(\cdot)_L$ and $(\cdot)_R$ denote the point values of the variable $(\cdot)$ at the points $(\xi_j, \eta_k)$ and $(\xi_{j+1}, \eta_k)$, respectively. If the pressure takes the form of $p = p(\rho, e)$, following the same course of reasoning as that used in [15], we can construct two matrices, $\boldsymbol{A}^{(1)}_{j+\frac{1}{2},k}$ and $\boldsymbol{A}^{(2)}_{j+\frac{1}{2},k}$, satisfying the following three properties

1. $\boldsymbol{A}^{(1)}_{j+\frac{1}{2},k} \to \frac{\partial \boldsymbol{F}_1}{\partial \boldsymbol{U}}$ and $\boldsymbol{A}^{(2)}_{j+\frac{1}{2},k} \to \frac{\partial \boldsymbol{F}_2}{\partial \boldsymbol{U}}$ as $\boldsymbol{U}_L \to \boldsymbol{U}_R \to \boldsymbol{U}$.

2. Each of the matrices $\boldsymbol{A}^{(1)}_{j+\frac{1}{2},k}$ and $\boldsymbol{A}^{(2)}_{j+\frac{1}{2},k}$ has four linearly independent eigenvectors.

3. $\boldsymbol{F}_1(\boldsymbol{U}_R) - \boldsymbol{F}_1(\boldsymbol{U}_L) = \boldsymbol{A}^{(1)}_{j+\frac{1}{2},k}(\boldsymbol{U}_R - \boldsymbol{U}_L)$ and $\boldsymbol{F}_2(\boldsymbol{U}_R) - \boldsymbol{F}_2(\boldsymbol{U}_L) = \boldsymbol{A}^{(2)}_{j+\frac{1}{2},k}(\boldsymbol{U}_R - \boldsymbol{U}_L)$.

As defined by (2.2a), $\boldsymbol{F}_1$ and $\boldsymbol{F}_2$ are nonlinear functions of $\boldsymbol{U}$ only. We assume that $X_\xi, X_\eta, Y_\xi$ and $Y_\eta$ denote the point values of $x_\xi, x_\eta, y_\xi$ and $y_\eta$ at the point $(\xi_{j+\frac{1}{2}}, \eta_k)$, respectively. The matrix $\boldsymbol{A}_{j+\frac{1}{2},k}$ is defined as

$$\boldsymbol{A}_{j+\frac{1}{2},k} = Y_\eta \boldsymbol{A}^{(1)}_{j+\frac{1}{2},k} - X_\eta \boldsymbol{A}^{(2)}_{j+\frac{1}{2},k}.$$

Assume that $\boldsymbol{A}_{j+\frac{1}{2},k} = \boldsymbol{R}_{j+\frac{1}{2},k}\boldsymbol{\Lambda}_{j+\frac{1}{2},k}\boldsymbol{L}_{j+\frac{1}{2},k}$, $\boldsymbol{R}_{j+\frac{1}{2},k} = [R_1, R_2, R_3, R_4]$ and $\boldsymbol{L}_{j+\frac{1}{2},k} = [L_1, L_2, L_3, L_4]$, we have the following results.

**Proposition A.1.** *The matrix $\boldsymbol{A}_{j+\frac{1}{2},k}$ is given by*

$$\begin{pmatrix}
0 & Y_\eta & -X_\eta & 0 \\
Y_\eta\left[\tilde{c}_s^2 - \frac{\widetilde{p_e}}{\tilde{\rho}}(\tilde{H} - \tilde{u}^2 - \tilde{v}^2)\right] - \tilde{u}\tilde{U} & \tilde{U} + Y_\eta\tilde{u}\left(1 - \frac{\widetilde{p_e}}{\tilde{\rho}}\right) & -X_\eta\tilde{u} - Y_\eta\tilde{v}\frac{\widetilde{p_e}}{\tilde{\rho}} & Y_\eta\frac{\widetilde{p_e}}{\tilde{\rho}} \\
-X_\eta\left[\tilde{c}_s^2 - \frac{\widetilde{p_e}}{\tilde{\rho}}(\tilde{H} - \tilde{u}^2 - \tilde{v}^2)\right] - \tilde{v}\tilde{U} & Y_\eta\tilde{v} + X_\eta\tilde{u}\frac{\widetilde{p_e}}{\tilde{\rho}} & \tilde{U} - X_\eta\tilde{v}\left(1 - \frac{\widetilde{p_e}}{\tilde{\rho}}\right) & -X_\eta\frac{\widetilde{p_e}}{\tilde{\rho}} \\
\tilde{U}\left[\tilde{c}_s^2 - \tilde{H} - \frac{\widetilde{p_e}}{\tilde{\rho}}(\tilde{H} - \tilde{u}^2 - \tilde{v}^2)\right] & Y_\eta\tilde{H} - \tilde{u}\tilde{U}\frac{\widetilde{p_e}}{\tilde{\rho}} & -X_\eta\tilde{H} - \tilde{v}\tilde{U}\frac{\widetilde{p_e}}{\tilde{\rho}} & \tilde{U}\left(1 + \frac{\widetilde{p_e}}{\tilde{\rho}}\right)
\end{pmatrix}$$

*with the eigenvalues*

$$\boldsymbol{\Lambda}_{j+\frac{1}{2},k} = \operatorname{diag}\left(\tilde{U} - \tilde{c}_s\sqrt{X_\eta^2 + Y_\eta^2},\ \tilde{U},\ \tilde{U},\ \tilde{U} + \tilde{c}_s\sqrt{X_\eta^2 + Y_\eta^2}\right),$$

*the corresponding right eigenvectors*

$$R_1 = \begin{pmatrix} 1 \\ \tilde{u} - \tilde{c}_s \frac{Y_\eta}{\sqrt{X_\eta^2+Y_\eta^2}} \\ \tilde{v} + \tilde{c}_s \frac{X_\eta}{\sqrt{X_\eta^2+Y_\eta^2}} \\ \tilde{H} - \tilde{c}_s \frac{\tilde{U}}{\sqrt{X_\eta^2+Y_\eta^2}} \end{pmatrix}, \quad R_2 = \begin{pmatrix} 1 \\ \tilde{u} \\ \tilde{v} \\ \tilde{H} - \frac{\tilde{\rho}}{\widetilde{p_e}}\tilde{c}_s^2 \end{pmatrix},$$

$$R_3 = \begin{pmatrix} 0 \\ X_\eta \\ Y_\eta \\ X_\eta \tilde{u} + Y_\eta \tilde{v} \end{pmatrix}, \quad R_4 = \begin{pmatrix} 1 \\ \tilde{u} + \tilde{c}_s \frac{Y_\eta}{\sqrt{X_\eta^2+Y_\eta^2}} \\ \tilde{v} - \tilde{c}_s \frac{X_\eta}{\sqrt{X_\eta^2+Y_\eta^2}} \\ \tilde{H} + \tilde{c}_s \frac{\tilde{U}}{\sqrt{X_\eta^2+Y_\eta^2}} \end{pmatrix},$$

*and the corresponding left eigenvectors*

$$L_1 = \frac{\widetilde{p_e}}{2\tilde{\rho}\tilde{c}_s^2\sqrt{X_\eta^2+Y_\eta^2}} \begin{pmatrix} \frac{\tilde{\rho}}{\widetilde{p_e}}\tilde{c}_s\left(\tilde{c}_s\sqrt{X_\eta^2+Y_\eta^2}+\tilde{U}\right) + \sqrt{X_\eta^2+Y_\eta^2}\left(\tilde{u}^2+\tilde{v}^2-\tilde{H}\right) \\ -\left(\tilde{u}\sqrt{X_\eta^2+Y_\eta^2} + \frac{\tilde{\rho}}{\widetilde{p_e}}\tilde{c}_s Y_\eta\right) \\ \frac{\tilde{\rho}}{\widetilde{p_e}}\tilde{c}_s X_\eta - \tilde{v}\sqrt{X_\eta^2+Y_\eta^2} \\ \sqrt{X_\eta^2+Y_\eta^2} \end{pmatrix}^\top,$$

$$L_2 = \frac{\widetilde{p_e}}{\tilde{\rho}\tilde{c}_s^2} \begin{pmatrix} \tilde{H} - \tilde{u}^2 - \tilde{v}^2 \\ \tilde{u} \\ \tilde{v} \\ -1 \end{pmatrix}^\top, \qquad L_3 = \frac{1}{X_\eta^2+Y_\eta^2} \begin{pmatrix} -\tilde{u}X_\eta - \tilde{v}Y_\eta \\ X_\eta \\ Y_\eta \\ 0 \end{pmatrix}^\top,$$

$$L_4 = \frac{\widetilde{p_e}}{2\tilde{\rho}\tilde{c}_s^2\sqrt{X_\eta^2+Y_\eta^2}} \begin{pmatrix} \frac{\tilde{\rho}}{\widetilde{p_e}}\tilde{c}_s\left(\tilde{c}_s\sqrt{X_\eta^2+Y_\eta^2}-\tilde{U}\right) + \sqrt{X_\eta^2+Y_\eta^2}\left(\tilde{u}^2+\tilde{v}^2-\tilde{H}\right) \\ -\tilde{u}\sqrt{X_\eta^2+Y_\eta^2} + \frac{\tilde{\rho}}{\widetilde{p_e}}\tilde{c}_s Y_\eta \\ -\left(\frac{\tilde{\rho}}{\widetilde{p_e}}\tilde{c}_s X_\eta + \tilde{v}\sqrt{X_\eta^2+Y_\eta^2}\right) \\ \sqrt{X_\eta^2+Y_\eta^2} \end{pmatrix}^\top.$$

*Here, the variables* $\tilde{u}$, $\tilde{v}$, $\tilde{e}$, $\tilde{H}$, $\tilde{\rho}$, $\tilde{U}$, $\tilde{p}$ *are given by*

$$\tilde{Z} = \frac{\sqrt{\rho_R}Z_R + \sqrt{\rho_L}Z_L}{\sqrt{\rho_R}+\sqrt{\rho_L}}, \quad Z = u,\, v,\, e,\, or\, H,$$

$$\tilde{\rho} = \sqrt{\rho_L\rho_R}, \quad \tilde{U} = \tilde{u}Y_\eta - \tilde{v}X_\eta, \quad \tilde{p} = \tilde{\rho}\left(\tilde{H} - \tilde{e} - \frac{1}{2}(\tilde{u}^2+\tilde{v}^2)\right),$$

*where the quantity* $H$ *denotes the enthalpy and is defined as* $H = p/\rho + e + (u^2+v^2)/2$. *The variables* $\tilde{c}_s$, $\widetilde{p_\rho}$, $\widetilde{p_e}$ *are taken as*

$$\tilde{c}_s = \sqrt{\widetilde{p_\rho} + \frac{\tilde{p}\widetilde{p_e}}{\tilde{\rho}^2}},$$

$$\widetilde{p_\rho} = \begin{cases} \frac{1}{2}\left[\frac{p(\rho_R,e_R)-p(\rho_L,e_R)}{\rho_R-\rho_L} + \frac{p(\rho_R,e_L)-p(\rho_L,e_L)}{\rho_R-\rho_L}\right], & \rho_L \neq \rho_R, \\ \frac{1}{2}\left[p_\rho(\rho,e_L) + p_\rho(\rho,e_R)\right], & \rho_L = \rho_R = \rho, \end{cases} \tag{A.1a}$$

$$\widetilde{p_e} = \begin{cases} \frac{1}{2}\left[\frac{p(\rho_R,e_R)-p(\rho_R,e_L)}{e_R-e_L} + \frac{p(\rho_L,e_R)-p(\rho_L,e_L)}{e_R-e_L}\right], & e_L \neq e_R, \\ \frac{1}{2}\left[p_e(\rho_L,e) + p_e(\rho_R,e)\right], & e_L = e_R = e, \end{cases} \tag{A.1b}$$

*with the abbreviations* $p_\rho = \partial p(\rho,e)/\partial\rho|_e$, $p_e = \partial p(\rho,e)/\partial e|_\rho$. *In the case of an ideal gas, equations* (A.1) *yield*

$$\widetilde{p_\rho} = (\gamma-1)\frac{1}{2}(e_L + e_R),$$
$$\widetilde{p_e} = (\gamma-1)\frac{1}{2}(\rho_L + \rho_R).$$